Nuclear Instruments and Methods in Physics Research A329 (1993) 79–111
North-Holland

NUCLEAR
INSTRUMENTS
& METHODS
IN PHYSICS
RESEARCH
Section A

The HERA polarimeter and the first observation of electron spin polarization at HERA

D.P. Barber [a], H.-D. Bremer [a], M. Böge [a], R. Brinkmann [a], W. Brückner [b], Ch. Büscher [b], M. Chapman [c], K. Coulter [d], P.P.J. Delheij [e], M. Düren [b], E. Gianfelice-Wendt [a], P.E.W. Green [f], H.G. Gaul [b], H. Gressmann [g], O. Häusser [e,h], R. Henderson [e], T. Janke [g], H. Kaiser [a], R. Kaiser [i], P. Kitching [f], R. Klanner [a], P. Levy [e], H.-Ch. Lewin [a], M. Lomperski [j], W. Lorenzon [k], L. Losev [l], R.D. McKeown [k], N. Meyners [a], B. Micheel [g], R. Milner [c], A. Mücklich [b], F. Neunreither [b], W.-D. Nowak [n], P.M. Patel [o], K. Rith [b], Ch. Scholz [b], E. Steffens [b], M. Veltri [b], M. Vetterli [e,h], W. Vogel [a], W. Wander [b], D. Westphal [g], K. Zapfe [b] and F. Zetsche [b]

[a] *Deutsches Elektronen-Synchrotron DESY, Hamburg, Germany*
[b] *Max Planck Institut für Kernphysik, Heidelberg, Germany*
[c] *Massachusetts Institute of Technology, Boston, USA*
[d] *Argonne National Laboratory, Argonne, USA*
[e] *TRIUMF, Vancouver, Canada*
[f] *University of Alberta, Edmonton, Canada*
[g] *University of Hamburg, Germany*
[h] *Simon Fraser University, Vancouver, Canada*
[i] *University of Münster, Germany*
[j] *University of Wisconsin, Madison, USA*
[k] *California Institute of Technology, Pasadena, USA*
[l] *Lebedev Physical Institute, Moscow, Russian Federation*
[n] *DESY - Institut für Hochenergiephysik, Zeuthen, Germany*
[o] *McGill University, Montreal, Canada*

Received 29 October 1992

Electron spin polarizations of about 8% were observed at HERA in November 1991. In runs during 1992, utilizing special orbit corrections, polarization values close to 60% have been achieved. In this paper the polarimeter, the machine conditions, the data analysis, the first results and plans for future measurements are described.

1. Introduction

This paper describes the HERA polarimeter and reports on the first measurements in November 1991 of radiative electron spin polarization at HERA. Results obtained during April–July 1992 [1] are also summarized.

HERA is the high energy electron–proton colliding beam facility that has been constructed at the Deutsches Elektronen-Synchrotron (DESY) laboratory in Hamburg, Germany [2]. The first electron–proton collisions were observed in October 1991 and the two high energy physics experiments ZEUS [3] and H1 [4] have been taking data since June 1992. The electrons and protons are stored in separate vacuum pipes 6336 m in circumference and with energies of up to 35 GeV and 820 GeV and design currents of 60 and 160 mA, respectively. The design luminosity at each interaction point is 1.5×10^{31} cm^{-2} s^{-1}. More details may be found in ref. [2]. HERA has been designed with the possibility of storing spin polarized electrons to provide longitudinally polarized electrons at the interaction points.

Loskutov, Korovina, Sokolov and Ternov [5] noticed that in a storage ring electrons can become polarized antiparallel to the guide field by the emission of synchrotron radiation. This is due to a small difference between the spin flip rates up-to-down and vice versa. Only a very small fraction of the synchrotron radiation power causes spin flip [6], so that the polarization

process tends to be slow on the time scale of other dynamical phenomena of storage rings. Unified quantum mechanical treatments of the polarization state of the beam taking into account single particle radiative and orbital effects have been given by Derbenev and Kondratenko [7] and by Mane [8]. For a survey of the current state of the theory and references to other treatments see [9].

Radiative polarization was first detected at ACO and Novosibirsk [10]. It has also been seen at CESR [11], SPEAR [12], VEPP2M and VEPP4 [13], and at the PETRA and DORIS rings [14] where vertical polarizations of over 70 and 80% at beam energies of 16.5 and 5.01 GeV, respectively, have been observed. In 1990 vertical polarization was also observed for the first time at LEP [15] and TRISTAN [16] at energies of about 46 GeV and 30 GeV, respectively. In this paper we discuss the first measurements of vertical polarization at HERA for the machine without the spin rotators [17] which are necessary to obtain longitudinal polarization at selected interaction points.

The polarization increases in time according to

$$P(t) = P_{\max}(1 - e^{-t/\tau}), \tag{1}$$

where τ is the polarization time and $P_{\max}$ is the equilibrium polarization; $P(0)$ is assumed to be 0. In a planar storage ring and in the absence of depolarizing effects the equilibrium polarization is $P_{ST} = 8/(5\sqrt{3}) = 92.4\%$ and the time constant for the exponential build up is [6]

$$\tau_{ST} = \left(\frac{5\sqrt{3}}{8} \frac{c\lambda_c r_0 \gamma^5}{C} \oint \frac{ds}{|\rho|^3} \right)^{-1}, \tag{2}$$

where γ is the Lorentz factor E_e/m_e; λ_c and r_0 are the reduced Compton wavelength and the classical radius, respectively, of the electron; ρ is the radius of curvature in the magnets; C is the ring circumference and s is the distance along the ring. At HERA the time constant τ_{ST} is 40 and 11 min at 27 and 35 GeV, respectively.

The polarization mechanism can be counteracted by strong depolarizing effects which increase with energy and can limit the achievable polarization. The chief source of the depolarization is again the emission of synchrotron radiation which stochastically excites oscillations in the particle orbits. In an ideal storage ring the polarization is antiparallel to the guiding field; in a real machine with closed orbit distortions the magnetic field on the closed orbit is not exactly vertical and the spin axis can be tilted by tens of milliradians. In the presence of stochastic orbit motion this causes a diffusion of the spins according to the Bargmann–Michel–Telegdi (BMT) equation [18], which leads to depolarization. The classical spin vector (in the rest frame) precesses around the magnetic field according to the BMT equation and the number of rotations in a single turn around the ring on the closed orbit is called the spin tune and is given by

$$\nu = a\gamma \tag{3}$$

$$= \frac{E(\text{GeV})}{0.440625}, \tag{4}$$

where $a = (g-2)/2$ and g is the g-factor of the electron. The depolarizing effects are strongest at the spin orbit resonances, i.e. when the natural precession motion is related to the orbital motion by

$$\nu = m + m_x Q_x + m_y Q_y + m_s Q_s, \tag{5}$$

where the m's are integers and Q_x, Q_y, and Q_s are, respectively, the horizontal, vertical and synchrotron tunes of the machine.

In the presence of depolarizing effects the maximum polarization and the build-up time are

$$P_{\max} = P_{ST} \frac{\tau_{dep}}{\tau_{ST} + \tau_{dep}}, \tag{6}$$

$$\tau = \tau_{ST} \frac{\tau_{dep}}{\tau_{ST} + \tau_{dep}}, \tag{7}$$

where the strength of the depolarization is described by the time constant τ_{dep}. For example at HERA at 27 GeV, with $\tau_{dep} = 10$ min the build-up time $\tau = 8$ min and $P_{\max} = 0.18$. The simple relation between $P_{\max}$ and τ allows for the check of the measured polarization scale with the measurement of $P_{\max}$ from a measurement of the rise time.

The depolarizing effects due to magnet misalignments and orbit errors can be minimized using orbit correction algorithms [19]. Predictions of the polarization can be made using the analytical theory [7,8] or Monte Carlo spin tracking calculations [20]. However, since the polarization is very sensitive to the exact distortion of the machine and since this distortion cannot be measured with sufficient accuracy, they serve only as a guide when setting up the machine and in correcting the orbit. Thus the orbit must be optimized empirically and this requires a fast polarimeter. A common method used in many high energy electron storage rings is Compton-laser polarimetry. This method has also been used at HERA.

In this paper we discuss the method of Compton-laser polarimetry, the design of the HERA polarimeter, the measurements made during the machine run of Nov. 1991 when the first conclusive evidence of polarization was seen, the analysis of these data and the results obtained. The results of measurements performed in April–June 1992 are also included, but the more recent measurements performed in August–October to optimize the orbit corrections will be described in another report.

2. Compton polarimetry

Compton-laser polarimeters, widely used at e^+e^- storage rings (LEP, TRISTAN, etc.), utilize the spin dependent cross section for Compton scattering of polarized photons on electrons: the scattering of circularly polarized photons (from a laser) on vertically polarized electrons is asymmetric with respect to the orbital plane of the electrons, and the magnitude of the asymmetry is proportional to the vertical polarization of the electrons. The longitudinal component of the electron polarization is measured through the energy dependence of the cross section. The polarization can be deduced from measurements of the final electron [21] but at storage rings it is more practical to detect the scattered photon.

To determine the electron polarization with an absolute accuracy of 1% requires approximately 10^6 scattered photons. The detection of individual photons is called the "single-photon" method. It can be used if the background from beam-gas bremsstrahlung is small and the time between electron bunches is short. Otherwise, the "multi-photon" method is more appropriate, when a pulsed high power laser is utilized to produce thousands of backscattered photons on each interaction with an electron bunch [22]. Compton scattering then dominates over the background and a high statistical accuracy can be reached in a short time. However, the single-photon method allows detailed crosschecks and diagnostics. This method has been adopted for the measurements at HERA, and we measure by scattering 2.41 eV laser photons in a continuous beam of 10 W off the electrons. In this section we describe the features of the polarization dependent Compton cross section and discuss the measurement of the vertical and longitudinal components of the electron polarization with the single-photon method; results for the multi-photon method are included for comparison.

2.1. The Compton cross section

The differential Compton cross section can be written as a function of the initial electron and photon polarizations $\boldsymbol{P}$ and $\boldsymbol{S}$ in the following way [23]:

$$\frac{d\sigma_c}{d\Omega}(S, P) = \Sigma_0 + \Sigma_1(S_1) + \Sigma_2(S_3, P), \tag{8}$$

where

$$\Sigma_0 = C\left[(1+\cos^2\theta) + (k_i - k_f)(1-\cos\theta)\right],$$
$$\Sigma_1(S_1) = CS_1(\phi)\sin^2\theta,$$
$$\Sigma_2(S_3, P) = -CS_3(\phi)(1-\cos\theta)(\boldsymbol{k}_i\cos\theta + \boldsymbol{k}_f)\cdot\boldsymbol{P},$$
$$C = 0.5 r_0^2 k_f^2 k_i^{-2},$$
$$k_i = 2\gamma E_\lambda / m_e,$$
$$k_f = 1/(1-\cos\theta + 1/k_i); \tag{9}$$

r_0 is the classical electron radius and E_λ is the laser photon energy in the lab frame. For the measurements reported here the laser photon energy E_λ is 2.41 eV and the nominal electron beam energy E_e is 26.6 GeV. These values will be used for the examples presented in this section. Eq. (8) is valid in the rest frame of the electron. The initial photon travels in the $+z$ direction; the y axis is normal to the plane of the storage ring and $+x$ is directed towards the center of the ring. The collision is head-on in the lab frame; see fig. 1. The angle ϕ is measured from the $+x$ axis towards $+y$. The rest frame momentum of the laser photon k_i is 0.49 and is directed along the z axis. The initial photon is scattered into (θ, ϕ) with final momentum $\boldsymbol{k}_f$. The total Compton scattering cross section σ_c is 376 mb. In the laboratory frame the photons are backscattered into a narrow cone centered on the direction of the initial electron: for example scattering at $\theta = 90°$ transforms to a laboratory scattering angle $\theta_{lab} = \gamma^{-1} = 20$ μrad and an energy $E_\gamma = 8.8$ GeV;

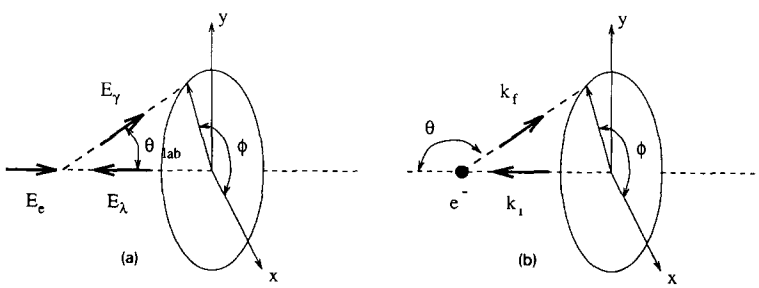

Fig. 1. Geometry and coordinate system of Compton scattering, showing the laboratory and rest frame scattering angles of the photon. The final electron is not shown.

scattering at $\theta = 180°$ transforms to $\theta_{lab} = 0°$ and $E_\gamma = 13.2$ GeV.

The polarization of the initial electron is specified in Cartesian coordinates by $\boldsymbol{P} = (P_X, P_Y, P_Z)$. The radiative polarization of the electrons in a perfectly aligned flat storage ring is antiparallel to the bending field, which in our reference frame is in the $-y$ direction and so $P_Y > 0$. Owing to imperfections in the storage ring geometry the spin axis may be tilted (up to ≈ 100 mrad) and therefore the components P_X and P_Z may be nonzero, but they are small compared with P_Y.

The polarization of the initial photon is specified using the Stokes vector [24] $\boldsymbol{S} = (S_0, S_1, S_2, S_3)$. The components are defined in the following way:

$$\begin{aligned} S_0 &= E_1^2 + E_2^2, \\ S_1 &= E_1^2 - E_2^2, \\ S_2 &= 2E_1E_2 \cos\delta, \\ S_3 &= 2E_1E_2 \sin\delta, \end{aligned} \tag{10}$$

where E_1 and E_2 are orthogonal components of the electric field whose phase difference is δ. For normalization of the Stokes vector we take $S_0 = 1$. In general, the total intensity of the light can be divided into linearly, circularly, and randomly polarized components. The magnitude of the linear polarization is $S_{lin} = \sqrt{S_1^2 + S_2^2}$ and the orientation of the polarization is specified by the azimuthal direction ϕ_{lin} of the electric field $\boldsymbol{E}_{lin}$; the method we use to measure S_{lin} and ϕ_{lin} is described in section 3.2.2. The magnitude of the circular polarization is $S_{circ} = |S_3|$. The sign of S_3 indicates the helicity of the polarization; we have adopted the convention that $S_3 < 0$ ($\sin\delta < 0$, the rotation of $\boldsymbol{E}$ and the direction of propagation form a right handed screw) denotes right handed helicity, and $S_3 > 0$ denotes left handed helicity. The degree of polarization of the light is $\mathscr{P} = \sqrt{S_1^2 + S_2^2 + S_3^2}$; the laser light is fully polarized so that $\mathscr{P} = 1$ and the magnitude of the circular polarization is obtained from measurements of S_{lin} with

$$S_{circ} = \sqrt{1 - S_{lin}^2}\,. \tag{11}$$

The directions of the vectors $\boldsymbol{E}_1$ and $\boldsymbol{E}_2$ are defined with respect to the scattering plane defined by the momenta $\boldsymbol{k}_i$ and $\boldsymbol{k}_f$: $\boldsymbol{E}_1$ is in the plane and $\boldsymbol{E}_2$ is perpendicular to the plane of scattering. The orientation of the plane is given by the azimuthal scattering angle ϕ, and as a result the electric field and Stokes components are functions of the angle ϕ. The electric field components are simply calculated for the scattering angle ϕ_{lin}: $\boldsymbol{E}_1 = \boldsymbol{E}_{lin}$ and $E_2 = 0$. It then follows that $S_1(\phi_{lin}) = E_1^2$ and $S_2(\phi_{lin}) = 0$ and so $S_1(\phi_{lin}) = S_{lin}$. The components of $\boldsymbol{S}$ associated with an arbitrary scattering angle ϕ can be calculated from $\boldsymbol{S}(\phi_{lin})$ using the following general coordinate rotation:

$$\begin{aligned} S_1(\phi_2) &= S_1(\phi_1)\cos 2(\phi_2 - \phi_1) \\ &\quad + S_2(\phi_1)\sin 2(\phi_2 - \phi_1), \\ S_2(\phi_2) &= -S_1(\phi_1)\sin 2(\phi_2 - \phi_1) \\ &\quad + S_2(\phi_1)\cos 2(\phi_2 - \phi_1), \\ S_3(\phi_2) &= S_3(\phi_1). \end{aligned} \tag{12}$$

We then reach the results that

$$S_1(\phi) = S_{lin}\cos 2(\phi - \phi_{lin}) \tag{13}$$

and S_3 is independent of ϕ.

The cross section term $\Sigma_1(S_1)$ in eq. (8) thus has a $\cos 2\phi$ modulation around the direction of the linear polarization ϕ_{lin}. To find an expression for this term without a direct dependence on the direction of the linear component we first calculate $\boldsymbol{S}(0)$. With eq. (12) the components are:

$$\begin{aligned} S_1(0) &= S_1(\phi_{lin})\cos(-2\phi_{lin}) + S_2(\phi_{lin})\sin(-2\phi_{lin}) \\ &= S_{lin}\cos 2\phi_{lin} \end{aligned} \tag{14}$$

$$\begin{aligned} S_2(0) &= -S_1(\phi_{lin})\sin(-2\phi_{lin}) + S_2(\phi_{lin}) \\ &\quad \times\cos(-2\phi_{lin}) \\ &= S_{lin}\sin 2\phi_{lin}. \end{aligned} \tag{15}$$

$S_1(\phi)$ is then obtained with an additional rotation of $(\phi_2 - \phi_1) = \phi$. Due to the large relative horizontal smearing of the backscattered distributions, only the vertical projections of the spatial distributions will be measured (see section 2.1.3). Thus summing over x, the expression for $S_1(\phi)$ can be simplified: summing the contributions of plus and minus x cancels the contributions of the $\sin 2\phi$ terms so that effectively

$$S_1(\phi) = S_1(0)\cos 2\phi. \tag{16}$$

Eq. (16) describes the effective azimuthal dependence of eq. (13) for projections onto the vertical axis: for linear polarizations oriented horizontally/vertically (i.e. $\phi_{lin} = 0°/90°$), $S_1(0) = +1/-1$ and the vertical projection of $\Sigma_1(S_1)$ is maximum, whereas for linear polarizations oriented at $\phi_{lin} = 45°$ and 135°, $S_1(0) = 0$ and the projection of $\Sigma_1(S_1)$ is zero, and thus the vertical projections of the backscattered distributions are identical to the case with unpolarized laser light.

We can then rewrite eq. (8) separating the terms with vertical and longitudinal components of the initial electron polarization and the measured linear and circular components of the initial photon polarization:

$$\frac{d\sigma_c}{d\Omega}(\boldsymbol{S}, \boldsymbol{P}) = \Sigma_0 + S_1(0)\Sigma_1' + S_3[P_Y\Sigma_{2Y} + P_Z\Sigma_{2Z}], \tag{17}$$

where

$$\Sigma_0 = C\left[(1+\cos^2\theta) + (k_1 - k_f)(1-\cos\theta)\right],$$

$$\Sigma_1' = C\cos 2\phi \sin^2\theta,$$

$$\Sigma_{2Y} = -Ck_f \sin\phi \sin\theta(1-\cos\theta),$$

$$\Sigma_{2Z} = -C(1-\cos\theta)(k_f + k_1)\cos\theta, \qquad (18)$$

and C is the common factor defined in eq. (9). S_3 and $S_1(0)$ are calculated from the measured quantities S_{lin} and ϕ_{lin} using eqs. (11) and (14). Because of the implicit summing over x in the derivation, eq. (17) is not a function of the electron polarization component P_X, and the linear polarization is specified by the measured value $S_1(0)$ with the effective azimuthal dependence of S_1 moved into the factor Σ_1'.

In the following subsections we describe the energy dependence and the effective azimuthal dependence of eq. (17). The projected vertical distributions are presented as functions of the photon energy E_γ, the laser polarization and the electron polarization. In section 2.2 we describe the methods used to obtain the vertical and longitudinal components of the electron polarization and the linear polarization of the laser light from the energy and vertical position distributions of the backscattered photons.

2.1.1. The energy dependence

When analyzing the Compton scattering of high energy electrons it is useful to consider the cross section as a function of the energy E_γ of the scattered photon in the lab frame and not of the rest frame scattering angle θ. The relation between these quantities is

$$\cos\theta = \frac{E_e - E_\gamma(1+1/k_1)}{E_e - E_\gamma}. \qquad (19)$$

The maximum scattered energy occurs at $\theta = 180°$ where

$$E_{\gamma,\max} = \frac{2E_e}{2+1/k_1}, \qquad (20)$$

which is 13.2 GeV with our initial conditions. Scattering in the rest frame at $\theta = 90°$ corresponds to $E_\gamma = 8.8$ GeV.

The energy spectrum $d\sigma_c/dE_\gamma$ (the differential cross section integrated over ϕ) of Compton scattering on unpolarized electrons is shown in fig. 2. Only the term Σ_0 contributes to the spectrum. If the electrons are longitudinally polarized and the laser light is circularly polarized ($S_3P_Z \neq 0$) then the term Σ_{2Z} contributes to the cross section, modifying the energy dependence. The energy spectra with $S_3P_Z = \pm 1$ are also shown in fig. 2. The measurement of P_Z using this effect is discussed in section 2.2.1.

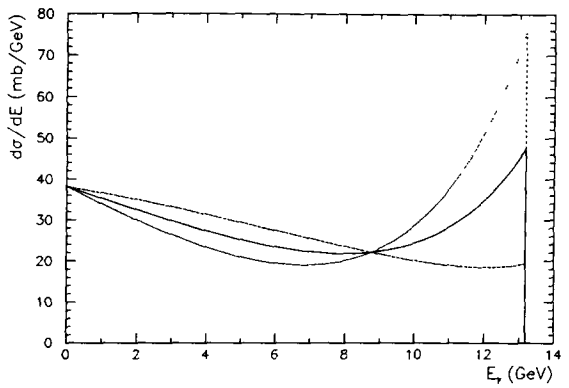

Fig. 2. Energy spectra of the scattered photon in the lab frame for Compton scattering. The solid curve is the spectrum for scattering with unpolarized electrons. Overlaid are the spectra for scattering with longitudinally polarized electrons for the cases of $S_3P_Z = +1$ (dashed curve) and $S_3P_Z = -1$ (dotted curve).

2.1.2. The azimuthal dependence

The unpolarized cross section Σ_0 does not depend on the azimuthal scattering angle ϕ, Σ_1' is proportional to $\cos 2\phi$ and Σ_{2Y} is proportional to $\sin\phi$. These azimuthal terms can be written as fractions of the unpolarized term Σ_0:

$$\frac{\Sigma_1'}{\Sigma_0} = Q_1 \cos 2\phi, \qquad (21)$$

$$\frac{\Sigma_{2Y}}{\Sigma_0} = Q_{2Y} \sin\phi. \qquad (22)$$

The dimensionless functions Q_1 and Q_{2Y} are shown in fig. 3 as functions of the energy E_γ. The term Σ_1' has a larger relative contribution to the total cross section than Σ_{2Y}, and both terms have maximum amplitudes near 9 GeV, corresponding to 90° scattering in the rest frame.

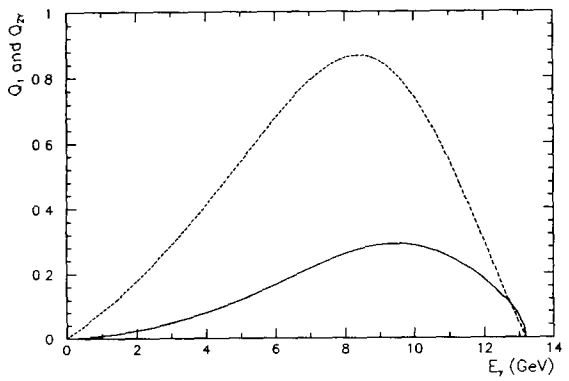

Fig. 3. The dimensionless functions Q_1 (dashed curve) and Q_{2Y} (solid curve) plotted as functions of the photon energy E_γ.

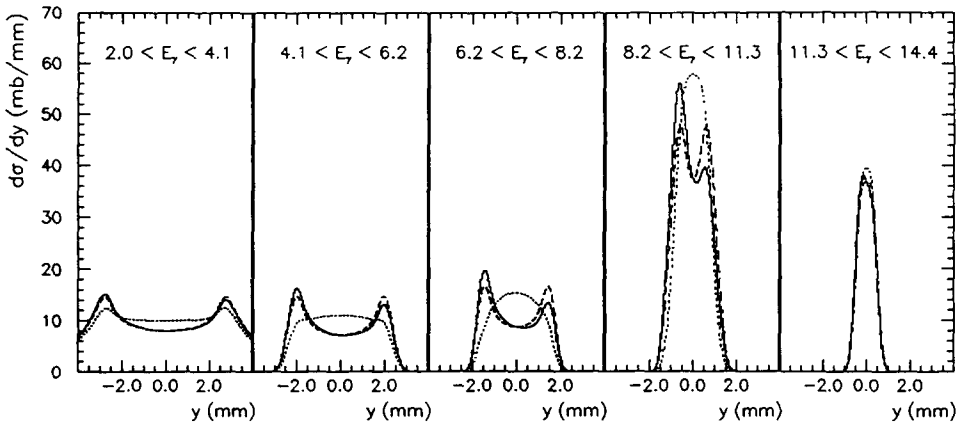

Fig. 4. Vertical Distributions $d\sigma_c/dy$ plotted versus y in five intervals ΔE_γ in E_γ. The distributions with two orientations of linear polarization are shown: the dashed curve corresponds to $\phi_{lin} = 45°$, $S_1(0) = 0$; and the dotted curve to $\phi_{lin} = 0°$, $S_1(0) = 1$. The solid curve corresponds to vertical electron and circular laser polarizations of $S_3 P_Y = 1$. The endpoints of the energy intervals are shown in the figure. Note that the range of the horizontal scales is ± 4 mm and the distributions in the first energy interval are truncated.

The measurement of the sin ϕ dependence of the vertical projections of the backscattered distributions gives the magnitude of $S_3 P_Y$, from which we obtain the vertical electron polarization P_Y. The measurement of the effective cos 2ϕ dependence gives the magnitude of $S_1(0)$, a measure of the linear polarization of the laser light. The methods used to obtain P_Y and $S_1(0)$ from the measured energy and vertical spatial distributions are discussed in section 2.2.

2.1.3. The divergence of the electron beam

The coordinate systems in fig. 1 describe the head-on collision of a photon and an electron. In practice there is a small crossing angle of the photon beam with respect to the z axis of the storage ring. [#1] More importantly the electrons at the interaction point (IP) are not all located at $x = y = 0$ traveling parallel to the z axis. In this section the effective smearing of the backscattered distributions due to the distributions in position and direction of the initial electrons is calculated.

The transverse positions x, y and directions x', y' with respect to the z axis of the electrons in a bunch are approximately Gaussian distributions with widths $\sigma_{e,x}$, $\sigma_{e,y}$ and $\sigma_{e,x'}$, $\sigma_{e,y'}$, respectively. The widths at the IP ($z = 0$) are related to the Twiss parameters [25] of the electron beam at that position:

$$\sigma_{e,y}(0) = \sqrt{\epsilon_y \beta_y(0)}\,, \tag{23}$$

$$\sigma_{e,y'}(0) = \sqrt{\epsilon_y \gamma_y(0)} = \sqrt{\epsilon_y \frac{1 + \alpha_y^2(0)}{\beta_y(0)}}\,. \tag{24}$$

[#1] At HERA the crossing angle α is 3.1 ± 0.2 mrad and can be neglected in the derivations in section 2.1.

The height of the electron beam a distance D from the IP (with no focussing elements between) is calculated in the following way:

$$\sigma_{e,y}(D) = \sqrt{\epsilon_y \beta_y(D)}$$
$$= \sqrt{\epsilon_y}\sqrt{\beta_y(0) - 2\alpha_y(0)D + \gamma_y(0)D^2}\,. \tag{25}$$

ϵ_y is the vertical emittance. Equivalent relations hold for x. The vertical and horizontal emittances are related by

$$\epsilon_y = K\epsilon_x\,, \tag{26}$$

where K is the coupling of the horizontal and vertical betatron motions. For the standard electron beam optic the Twiss parameters at the IP are $\alpha_x(0) = -0.04$, $\beta_x(0) = 14.8$ m and $\alpha_y(0) = 0.68$, $\beta_y(0) = 43.4$ m. The horizontal emittance ϵ_x is approximately 0.04 mm mrad. K is not accurately known but it is small; we use the estimate $K = 0.03$ (see section 5.4). Thus at the IP $\sigma_{e,x} = 0.77$ mm and $\sigma_{e,y} = 0.23$ mm; $\sigma_{e,x'} = 52$ μrad and $\sigma_{e,y'} = 6.4$ μrad. The width of the electron beam is significantly greater than its height, and so by crossing the laser beam through the electron beam from above one minimizes the sensitivity of the luminosity to drifts in the positions of the laser and electron beams at the IP (see sections 3.2.3 and 5.2.1).

The transverse momentum of the initial photon is negligible compared to that of the electron: therefore the z axis in fig. 1 is effectively the direction of the initial electron. The distribution of initial electron directions produces a smearing of the scattered photon distribution given by the projected size of the electron beam at the detector. The distance D from the IP to the detector is 65 m, and there the spot sizes $\sigma_{e,x}(65)$ and $\sigma_{e,y}(65)$ are 3.5 mm and 0.3 mm, respectively. Thus the horizontal smearing of the backscattered distribu-

tions is much larger than the vertical smearing making the measurement of the x dependence of the cross sections more difficult than of the y dependence. For this reason the measurement of the sin ϕ dependence of the scattering cross section (from which we obtain P_Y) is measured through projections of the backscattered distributions onto the y axis. The horizontal components of the electron spin vector, P_X, will not be measured. The detector is positioned at the maximum distance from the IP within the constraints of the tunnel geometry. The Twiss parameters of the electron beam at the IP have been chosen (within the constraints of the beam optics) for the optimal vertical "focus" of the backscattered photon beam at the position of the detector, by minimizing the vertical spot size of the projected electron beam relative to the size of the unsmeared backscattered photon beam.

2.1.4. Vertical projections

The y position at the detector of a photon scattered into (θ, ϕ) is given by:

$$y(\phi, E_\gamma) = R(E_\gamma) \sin \phi = \frac{D \sin \phi}{\gamma \tan \theta/2}, \tag{27}$$

where $R(E_\gamma) = D \tan \theta_{\text{lab}}$. For scattering at $\theta = 90°$ the final photon energy in the lab frame is $E_\gamma = 8.8$ GeV and $R = 1.2$ mm ($\theta_{\text{lab}} = \gamma^{-1} = 20$ μrad).

Vertical distributions $\mathrm{d}\sigma_c/\mathrm{d}y$ are shown in fig. 4. The smearing $\sigma_{e,y}(65)$ due to the vertical emittance of the electron beam has been included. A uniform distribution in ϕ (e.g. from the unpolarized term Σ_0) is a symmetric double-peaked distribution when projected onto the vertical axis. As the energy increases R decreases and the distributions become narrower in y. The energy dependence of the vertical distributions is shown by integrating the two-dimensional function over selected intervals ΔE_γ in energy,

$$\frac{\mathrm{d}\sigma_c}{\mathrm{d}y} = \int_{\Delta E_\gamma} \frac{\mathrm{d}^2\sigma_c}{\mathrm{d}y\ \mathrm{d}E_\gamma} \mathrm{d}E_\gamma, \tag{28}$$

and plotting the spectra $\mathrm{d}\sigma_c/\mathrm{d}y$ as functions of y. We have divided the Compton energy spectrum into the following five intervals ΔE_i (in GeV): $(E_{\min}, E_{\max})_i = (2.0, 4.1)_1$; $(4.1, 6.2)_2$; $(6.2, 8.2)_3$; $(8.2, 11.3)_4$; and $(11.3, 14.4)_5$. These intervals will be used in the remainder of this paper for showing the energy dependence of vertical distributions.

The effects of linear photon polarization on the scattered distributions are illustrated in fig. 4 by examples of scattering with linear polarization oriented at $\phi_{\text{lin}} = 45°$ (the dashed curve, for $S_1(0) = 0$ thus $\mathrm{d}\sigma_c/\mathrm{d}y = \Sigma_0$) and at $\phi_{\text{lin}} = 0°$ (the dotted curve, for $S_1(0) = 1$ thus $\mathrm{d}\sigma_c/\mathrm{d}y = \Sigma_0 + \Sigma_1'$). The contribution of Σ_1' to the vertical distribution is largest at $\phi = 0°$, 180° and (of the opposite sign) at $\phi = 90°$, 270°; thus the vertical distributions are narrower with horizontal photon polarization ($S_1(0) = +1$) and wider with vertically polarized laser light ($S_1(0) = -1$, not shown in the figure).

An example distribution with circular photon polarization and vertical electron polarization (the solid curve, for $S_3 P_Y = 1$ thus $\mathrm{d}\sigma_c/\mathrm{d}y = \Sigma_0 + \Sigma_{2Y}$) is also shown. The contribution of Σ_{2Y} is largest at $\phi = 90°$ and (of the opposite sign) at $\phi = 270°$. Thus the distributions from scattering circularly polarized photons on vertically polarized electrons ($S_3 P_Y \neq 0$) have an asymmetry with respect to the mid-plane $y = 0$: with $S_3 P_Y > 0$ there is an effective shift of the cross section from $+y$ to $-y$. The changes in the distributions introduced by the photon and electron polarizations are largest in the third and fourth energy intervals, as expected from the energy dependence of Q_1 and Q_{2Y}.

Note that the asymmetry functions $\Sigma_{1/0}'$ and $\Sigma_{2Y/0}$ which are defined in section 2.2.2 are shown in fig. 5 to facilitate the comparison with the vertical distributions plotted in fig. 4.

2.2. Cross section asymmetries

The degree of vertical electron polarization is obtained by measuring the asymmetry with respect to the plane of the storage ring of the scattering of circularly polarized light off the electrons. The asymmetry of the scattering rate measured, for example, with left polarized light ($S_3 = +1$) is

$$\mathscr{A}(y, E_\gamma) = \frac{N_L(y, E_\gamma) - N_L(-y, E_\gamma)}{N_L(y, E_\gamma) + N_L(-y, E_\gamma)} \tag{29}$$

$$= P_Y \frac{\Sigma_{2Y}}{\Sigma_0}, \tag{30}$$

where $N_L(y, E_\gamma)$ is the number of photons with energy between E_γ and $E_\gamma + \Delta E_\gamma$ at a vertical position between y and $y + \Delta y$. The asymmetry produced by the term Σ_{2Y} is visible in the distributions in fig. 4 with the maximum effect occurring in the third and fourth energy intervals. Linear polarization does not produce such an asymmetry. The center of the backscattered distribution ($y = 0$) is difficult to determine if the electron beam or the detector move during the measurement. This problem can be solved by measuring the asymmetry at the same vertical position of the backscattered distributions with opposite laser light helicities ($S_3 = \pm 1$, or left and right helicities):

$$\mathscr{A}(y, E_\gamma) = \frac{N_L(y, E_\gamma) - N_R(y, E_\gamma)}{N_L(y, E_\gamma) + N_R(y, E_\gamma)}. \tag{31}$$

This asymmetry is also described by eq. (30). The systematic effects of drifts during the individual measurements can be eliminated by frequently switching between the photon polarization states. One can ob-

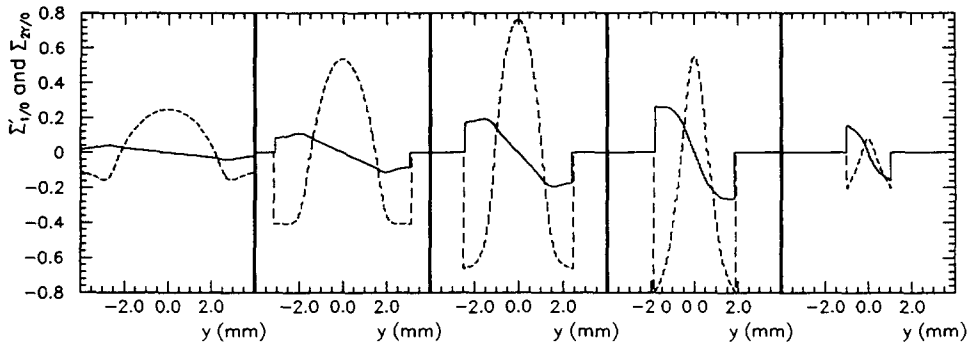

Fig. 5. The vertical asymmetry functions $\Sigma'_{1/0}$ (dashed curve, $\Delta S_1 = 1$) and $\Sigma_{2Y/0}$ (solid curve, $\Delta S_3 P_Y = 1$) plotted as functions of y in the five energy intervals. The functions are defined in section 2.2.2; the vertical distributions are positioned above for reference.

tain in addition the longitudinal component of the polarization P_Z from this asymmetry measurement.

The asymmetry of the cross sections for scattering with two arbitrary photon polarizations $S_a = (S_{1a}, S_{3a})$ and $S_b = (S_{1b}, S_{3b})$ is

$$\mathscr{A}(y, E_\gamma) = \frac{\sigma_a(y, E_\gamma) - \sigma_b(y, E_\gamma)}{\sigma_a(y, E_\gamma) + \sigma_b(y, E_\gamma)} \tag{32}$$

$$= \{(S_{1a} - S_{1b})\Sigma'_1 + (S_{3a} - S_{3b})[P_Y\Sigma_{2Y} + P_Z\Sigma_{2Z}]\} \times \{2\Sigma_0 + (S_{1a} + S_{1b})\Sigma'_1 + (S_{3a} + S_{3b})[P_Y\Sigma_{2Y} + P_Z\Sigma_{2Z}]\}^{-1} \tag{33}$$

$$= \frac{\Delta S_1\Sigma'_1 + \Delta S_3[P_Y\Sigma_{2Y} + P_Z\Sigma_{2Z}]}{\Sigma_0 + \bar{S}_1\Sigma'_1 + \bar{S}_3[P_Y\Sigma_{2Y} + P_Z\Sigma_{2Z}]}, \tag{34}$$

where $\Delta S_1 = (S_{1a} - S_{1b})/2$ and $\bar{S}_1 = (S_{1a} + S_{1b})/2$, with the equivalent relations for ΔS_3 and $\bar{S}_3$.

The optimal pairs of initial photon polarizations a and b to maximize the measured asymmetry for a given electron polarization correspond to ΔS_1 and $\Delta S_3 \approx 1$ which implies $\bar{S}_1 \approx \bar{S}_3 \approx 0$. For example, the maximum asymmetry with vertical electron polarization is reached when $\Delta S_3 \approx 1$ indicating that the linear components are small ($\bar{S}_1 \approx 0$) and the circular components are of opposite sign ($\bar{S}_3 \approx 0$). Because the values are small [#2] and the asymmetry does not depend strongly on them, we will take $\bar{S}_1 = \bar{S}_3 = 0$. The asymmetry distributions can then be written in the simple form

$$\mathscr{A}(y, E_\gamma) = \Delta S_1 \frac{\Sigma'_1}{\Sigma_0} + \Delta S_3 \left[P_Y \frac{\Sigma_{2Y}}{\Sigma_0} + P_Z \frac{\Sigma_{2Z}}{\Sigma_0} \right]. \tag{35}$$

In the following subsections the three terms of this function are described and their use in the measurement of the electron and laser photon polarizations is discussed. In section 2.2.3 the measurement of the vertical electron polarization from the shift of the mean vertical position of the backscattered distributions is described.

2.2.1. The energy asymmetry function

The energy spectra with longitudinal electron polarization $P_Z = 1$ and photon polarization $S_3 = \pm 1$ are shown in fig. 2. The integrals of Σ'_1 and Σ_{2Y} over y are zero so the general form of the asymmetry of energy spectra (following the derivation of eq. (35)) can be written as

$$\mathscr{A}(E_\gamma) = \frac{N_L(E_\gamma) - N_R(E_\gamma)}{N_L(E_\gamma) + N_R(E_\gamma)} = \Delta S_3 P_Z \frac{\int_y \Sigma_{2Z}\, dy}{\int_y \Sigma_0\, dy} = \Delta S_3 P_Z \Sigma_{2Z/0}. \tag{36}$$

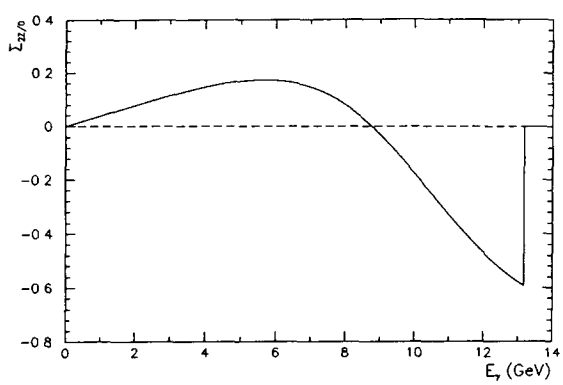

Fig. 6. The energy asymmetry function $\Sigma_{2Z/0}$ plotted versus the photon energy E_γ.

[#2] During our polarization measurements typically $\bar{S}_1 \approx -0.03$ and $\bar{S}_3 \approx 0.002$.

The energy asymmetry function $\Sigma_{2Z/0}$ is shown in fig. 6 The longitudinal polarization P_Z is obtained by fitting the measured energy asymmetry with eq. (36) with $\Delta S_3 P_Z$ as free parameter. Independent measurements of ΔS_3 are needed to isolate the longitudinal component P_Z.

2.2.2. The vertical asymmetry functions

The polarization component P_Y is measured using the two-dimensional asymmetry distribution $\mathscr{A}(y, E_\gamma)$ described in eq. (35) by selecting an energy interval ΔE_γ and studying the asymmetry $\mathscr{A}$ as a function of y. The term Σ_{2Z}/Σ_0 is independent of y and therefore it contributes an energy dependent constant to the function $\mathscr{A}(y)$ if $\Delta S_3 P_Z \neq 0$. The longitudinal polarization is expected to be small and can therefore be neglected when calculating the vertical distributions. We can then write the vertical asymmetry as

$$\mathscr{A}(y) = \Delta S_1 \frac{\int_{\Delta E_\gamma} \Sigma_1' \, dE_\gamma}{\int_{\Delta E_\gamma} \Sigma_0 \, dE_\gamma} + \Delta S_3 P_Y \frac{\int_{\Delta E_\gamma} \Sigma_{2Y} \, dE_\gamma}{\int_{\Delta E_\gamma} \Sigma_0 \, dE_\gamma}$$

$$= \Delta S_1 \Sigma_{1/0}' + \Delta S_3 P_Y \Sigma_{2Y/0}. \qquad (37)$$

The vertical asymmetry functions $\Sigma_{1/0}'$ and $\Sigma_{2Y/0}$ are shown in fig. 5, and the energy intervals ΔE_i defined in section 2.1.4 have been used in the calculation. The energy dependence of the asymmetry functions is qualitatively described by the functions $Q_1(E_\gamma)$ and $Q_{2Y}(E_\gamma)$ (section 2.1.2), which describe the maximum value of the vertical asymmetry $\mathscr{A}(y)$ at an energy E_γ.

The measured vertical asymmetry distributions are linear combinations of the two functions shown in fig. 5. The vertical polarization P_Y is obtained by fitting the measured vertical asymmetry distributions to eq. (37) with ΔS_1 and $\Delta S_3 P_Y$ as free parameters. In this fit the contribution to the asymmetry of the linear polarizations of the initial photons, ΔS_1, is also found. The correlation between the two components in the fit is zero because the function $\Sigma_{1/0}'$ is an even function of y while $\Sigma_{2Y/0}$ is odd.

Measurements with linearly polarized laser light ($S_3 = 0$) are independent of the electron polarization and the asymmetry $\mathscr{A}(y)$ is determined by the orientation of the linear polarizations, smearing by the electron beam, and detector resolutions. The vertical asymmetry function $\Sigma_{1/0}'$ is large and it is possible to accurately compare the shapes of the measured and predicted distributions. The value of ΔS_1 from the fit can be compared with the value from independent measurements of the polarizations of the laser light.

2.2.3. The shift in the means

Another way to measure the vertical electron polarization is to measure the shift of the mean vertical position of the backscattered photon distributions when the polarization of the laser light is switched between left and right circular polarizations:

$$\Delta y(E_\gamma) = \frac{\langle y \rangle_L - \langle y \rangle_R}{2} = \Delta S_3 P_Y \Pi(E_\gamma) \qquad (38)$$

where $\Pi(E_\gamma)$, often referred to as the analyzing power, is equal to the shift measured when $\Delta S_3 P_Y = 1$. The analyzing power is plotted as a function of the energy E_γ in fig. 7. The vertical polarization P_Y is obtained by fitting the measured shift $\Delta y(E_\gamma)$ to eq. (38) with $\Delta S_3 P_Y$ as free parameter. The analyzing power for the energy interval between 5.2 and 11.9 GeV is 142 μm. It is important to verify the expected energy dependence in measurements of Δy to be sure that the effect is indeed due to vertical electron polarization and is not an instrumental effect. However, for on-line purposes the measurement of the shift in a single energy interval with high analyzing power provides a simple and accurate method for extracting the vertical electron polarization.

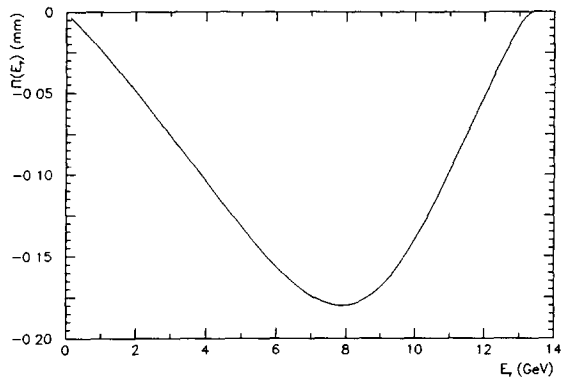

Fig. 7. The analyzing power $\Pi(E_\gamma)$ plotted as a function of E_γ.

2.3. Measurement errors

The longitudinal component of the electron polarization P_Z is measured through the asymmetry of the energy spectra (eq. (36)) and the vertical component P_Y through the vertical asymmetry distributions (eq. (37)) and through the mean shifts (eq. (38)). The magnitude of the asymmetries occuring in the measurement of electron polarization can be very small: with a vertical electron polarization $P_Y = 0.1$ the maximum asymmetry $\mathscr{A}(y, E_\gamma)$ is only ≈ 0.03. Therefore a large number of photons is required for a polarization measurement with small statistical error. To quantify the problem we will discuss the measurement of the vertical electron polarization from the mean shift Δy in the

energy interval between 5.2 and 11.9 GeV. The polarization is given by

$$P_Y = \frac{\Delta y}{\Delta S_3 \Pi} \tag{39}$$

and the statistical error δP_Y is then

$$\delta P_Y = \frac{1}{\Delta S_3 \Pi} \frac{\sigma_y}{\sqrt{N}}, \tag{40}$$

where σ_y is the rms width of the scattered distributions and $N = N_L + N_R$ is the total number of photons used to define the mean positions. The error of ΔS_3 has been neglected.

The analyzing power Π for the interval is 142 μm and the width σ_y is 1.02 mm. To achieve a statistical accuracy δP_Y of 0.01 requires $N = 5.2 \times 10^5$ photons in the energy interval and hence a total number of backscattered photons of 1.2×10^6. To collect enough photons in a short time requires a high average trigger rate, which might not be achievable without a significant contamination of multiple photons. In that case it would be wise to measure the vertical polarization utilizing the multi-photon technique. The design backscattering rate for the HERA polarimeter with the full electron current of 60 mA in 210 bunches is 100 kHz. At this rate the probability for double Compton scattering in a single bunch is only 1% and a statistical accuracy δP_Y of 0.01 is achieved in 12 s.

The measured polarization scale is sensitive to systematic errors. An independent way to calibrate the polarimeter is to measure the rise time of the polarization, eq. (1). If the build-up time is very short or if the polarization is small then this method is difficult to apply. The detailed measurement of the backscattered distribution allows for checks of the scale of the measured polarization, with measurement of the vertical asymmetry function $\Sigma'_{1/0}$ and two methods to measure the vertical electron polarization.

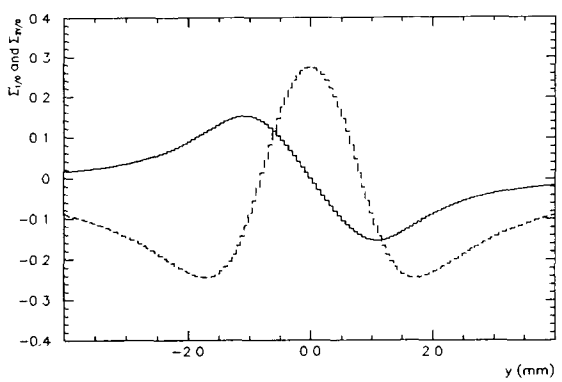

Fig. 8. The vertical asymmetry functions for measurements utilizing the multi-photon technique with $E_\lambda = 2.33$ eV. Plotted are $\Sigma'_{1/0}$ (the dashed curve, $\Delta S_1 = 1$) and $\Sigma_{2Y/0}$ (the solid curve, $\Delta S_3 P_Y = 1$) plotted as functions of y.

2.4. The multi-photon method

The multi-photon method [15] is used for polarization measurements when the background from the storage ring is large and/or when a statistically accurate single-photon measurement requires too much time. A pulsed high power laser is used to produce many backscattered photons in each interaction with an electron bunch. The photon energy spectrum is effectively integrated, and the energy dependence of the cross section cannot be measured. The results for the multi-photon technique are included to allow a comparison with the single-photon technique. Multi-photon measurements can be made utilizing frequency-doubled Nd:YAG lasers. The initial photon energy E_λ is 2.33 eV; the results presented in this section are calculated for this initial energy.

The asymmetry functions $\Sigma'_{1/0}$ and $\Sigma_{2Y/0}$ defined in eq. (37) are shown in fig. 8, with the energy interval ΔE_γ covering the full energy spectrum. The analyzing power Π is 94 μm. The asymmetries are smaller than the asymmetries obtained with the single-photon technique because the low and high energy regions dilute the maximum asymmetry in the middle energy range.

3. The HERA polarimeter

3.1. The layout

A schematic overview of the polarimeter is shown in fig. 9. This figure is a useful reference for the following sections in which the accelerator layout, the optical system, the calorimeter, and the data acquisition system are described.

A schematic layout of the storage ring in the region of the polarimeter is shown in fig. 10. The electron–photon interaction point (IP) is at the end of the West straight section at WR-134, just before the electron beam enters the arc. The laser and data acquisition electronics are located in the West Hall.

The accelerator layout in this area was designed expressly for the installation of the polarimeter [26] with two weak dipoles (type BC with $\rho = 3215$ m; see fig. 10) isolating a 4 m straight section from the large background produced in the straight section of the West Hall (360 m) and in the arcs (type BB with $\rho = 608$ m; see fig. 10). In a previous run [27] the background conditions were measured, including beam-gas bremsstrahlung and the synchrotron radiation produced in the weak dipoles. The measured vacuum pressure was about 2×10^{-8} mbar. For an optimal signal-to-background ratio an improvement in

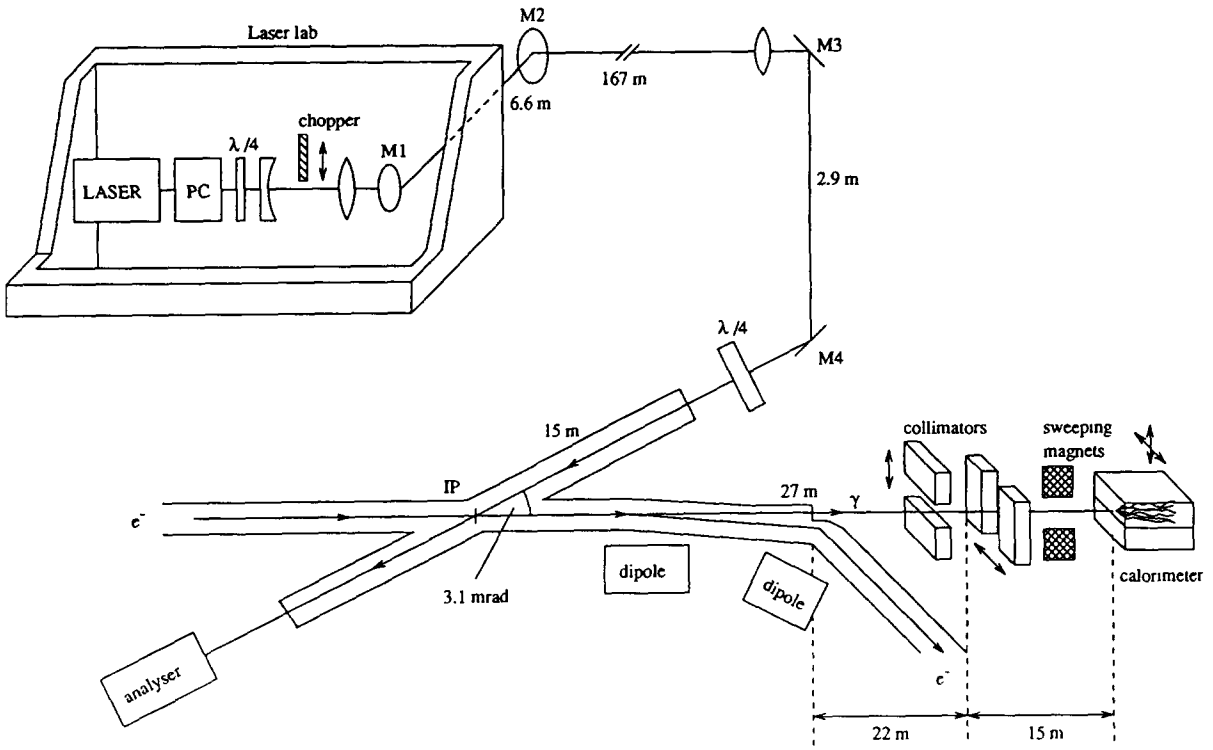

Fig. 9. An overview of the HERA polarimeter.

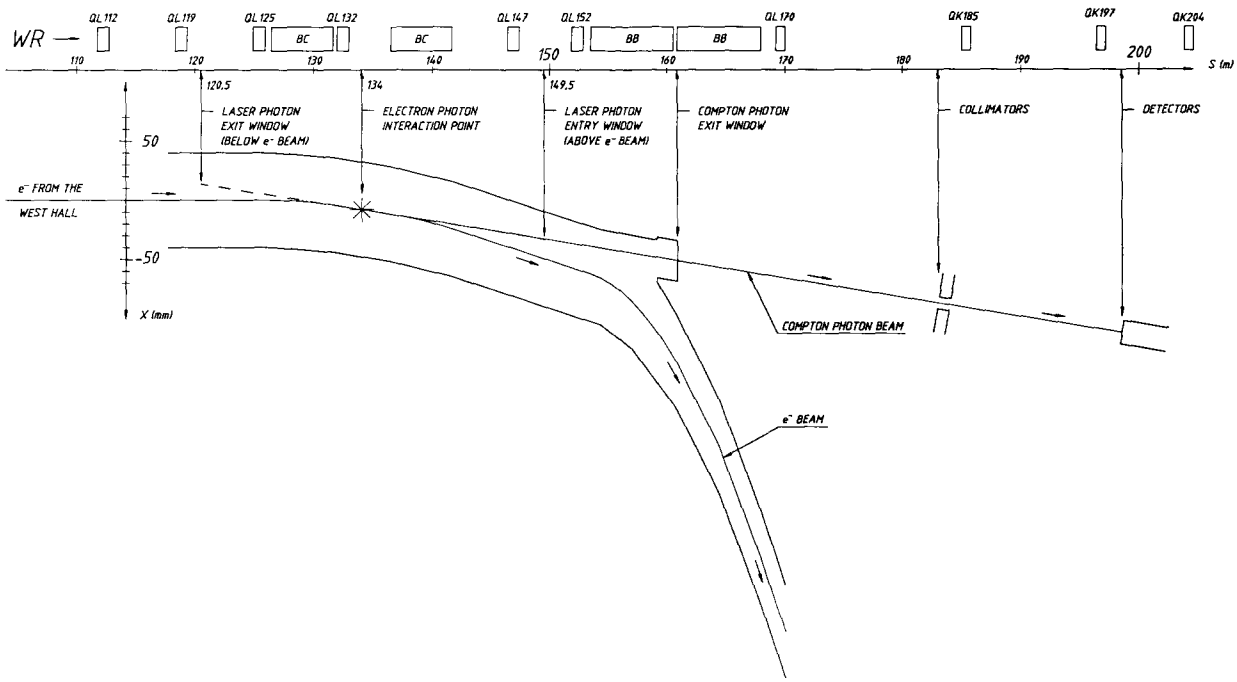

Fig. 10. Layout of the HERA storage ring in the region of the HERA polarimeter. The vacuum chamber is shown from above, indicating the entry and exit positions of the laser photons and the exit of the backscattered Compton photons. The magnet lattice is shown for reference.

the pressure of a factor between 10 and 100 was desired so additional vacuum pumps were added to the section.

The backscattered photons leave the IP traveling in the same direction as the electron beam. The two beams are first separated by the second weak dipole. After passing through the first strong dipole of the arc the beams have been separated enough for the photons to exit the vacuum chamber through a 0.5 mm thick aluminum window. The yokes of the dipoles are on the inside of the ring thus allowing for the installation of the special exit window. The detector is located at WR-200, 65 m from the IP, and is protected with lead shielding. It is placed as far from the IP as possible to increase the vertical size of the photon distributions at the face of the detector. A quadrupole (QL132, fig. 10) located between the weak dipoles vertically focuses the projected spot of the electron beam on the detector. To reject background not originating from the IP, vertical and horizontal collimators are placed 16 m upstream from the detector, followed by sweeping magnets to help remove any secondary electrons which are produced.

3.2. The optical system

An overview of the optical system is shown in fig. 11, and is discussed in the following subsections. For more details refer to ref. [28].

3.2.1. The laser beam transport system

The laser we have chosen is a 25 W Argon ion laser (INNOVA-200, Coherent Corporation). For electron polarization measurements a continuous 10 W beam of 2.41 eV (514.5 nm, green) photons is used. The laser is located in the West Hall and the laser beam is steered to the IP by means of four dielectric mirrors. The laser is mounted in the optical lab parallel to the electron beam at the height of the tunnel ceiling. The first mirror M1 deflects the beam by 90° into the tunnel and another deflection of 90° at M2 directs the beam 170 m through the tunnel to M3. The latter mirror deflects the beam from the tunnel ceiling down to the electron ring and M4 directs the beam through the entrance window into the electron vacuum chamber. After passing through the IP the beam exits the chamber through a second vacuum window and enters a polarization analyzer. A chopper (shutter) is mounted on the laser table to block the beam for background measurements.

In more commonly used chamber designs the laser beam enters the vacuum chamber perpendicularly to the direction of the electron beam and a vacuum mirror (or prism) reflects the laser beam against the electron beam at a small angle. Optical components which are in the electron vacuum are susceptible to damage by the electron beam and synchrotron radiation. Metal mirrors are typically used, and these have poor optical quality. For this reason it was decided to mount mirror M4 outside of the vacuum and use a high reflectivity dielectric mirror at this position. A fifth

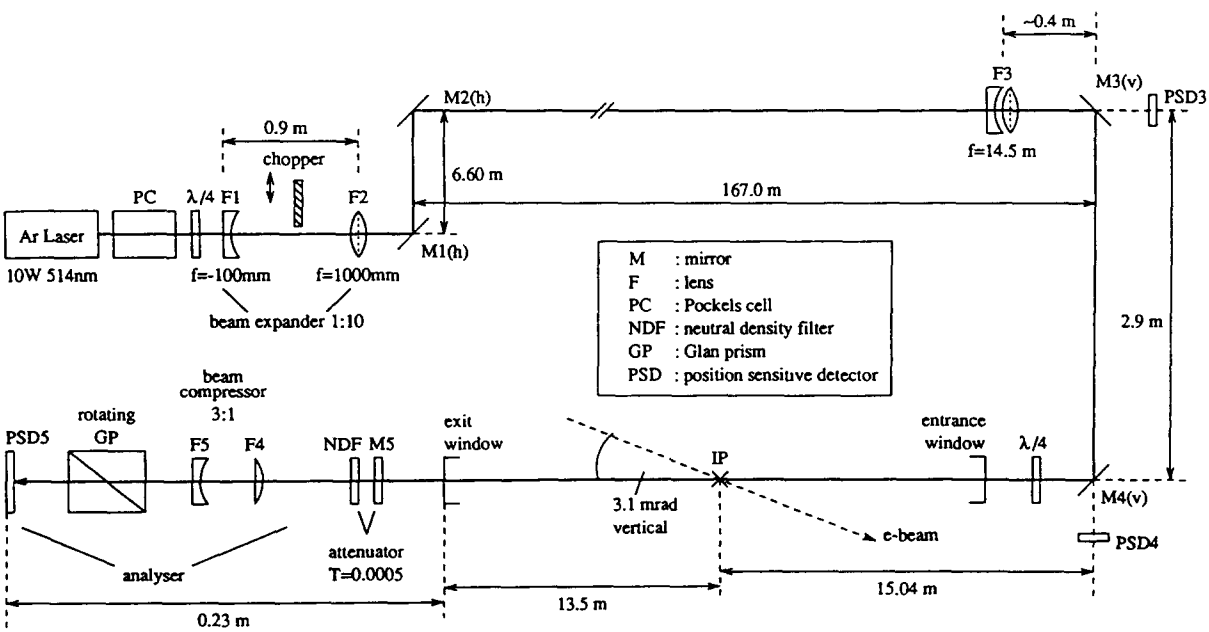

Fig. 11. An overview of the optical system.

mirror is not needed to reflect the beam out of the vacuum chamber into the polarization analyzer. Additional advantages are that mirrors do not need to be moved before electron injection and the replacement of optical components does not require breaking the machine vacuum.

Between the mirrors the laser beam is enclosed in an aluminum pipe of 150 mm diameter. Between M2 and M3 the pipe is mounted to the ceiling of the tunnel. The pipe is evacuated to a pressure of 1 to 10 mbar to reduce the fluctuations in the air density and thus improve the stability of the beam position. The laser beam passes through eight windows including the entrance and exit windows of the electron vacuum chamber. All windows have antireflection coatings. The entrance and exit windows to the electron vacuum chamber are vertically offset ≈ 45 mm from the electron beam and are nearly perpendicular to the beam direction. To withstand the background radiation they are 1 cm thick radiation resistant fused silica, glass type BK-7. Great care was taken in the construction of the vacuum windows, including stress-checks for birefringence produced by nonuniform stress in the glass.

Because of the long transport distance the mirror mounts must be very stable and must be adjusted to an accuracy of 2 μrad. For mounts M2 and M3 stepper-motor mounts were chosen from Aerotech Inc. [#3]. They are computer controlled and have a minimum step size of 0.2 μrad. The resonant frequencies of the mounts are greater than 200 Hz. Mounts M1 and M4 are adjusted by hand.

To facilitate the transport of the beam a Galilean lens system with a magnification factor of 10 is used in the laser lab to increase the size of the beam and decrease its divergence. The beam is focussed at the IP by the lens F3, which is mounted in front of M3. A double-lens system with an effective focal length of 14.5 m is used. The matrix for the transport of the beam from the laser to the IP is nearly unity. The size of the beam at the IP can be changed by adjusting the position of F1. The measured size is $\sigma_\gamma \approx 0.6$ mm.

The mirrors must be precisely positioned to thread the beam through the 200 m transport system. Video cameras are located after M2, before M3 and at M4 to give qualitative information about the beam alignment. Two diaphragms and a movable target near M3 aid in the positioning of M2. The small fraction of the laser light which is transmitted through the dielectric mirrors is measured by position sensitive detectors (PSDs) to provide precise monitoring of the beam position.

3.2.2. The polarization of the laser light

For the measurement of the electron polarization left and right circularly polarized light are scattered off the electron beam. The laser light is initially linearly polarized ($S_{\text{lin}} > 0.99$), and the polarization is changed using a Pockels cell and quarter-wave ($\lambda/4$) plates. The polarization state of the light is switched at 90 Hz by switching the high voltage on the Pockels cell with a pulse generator.

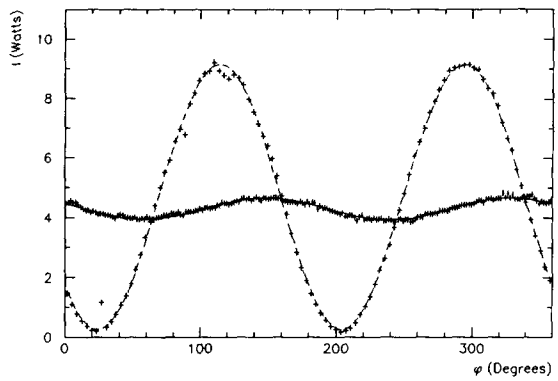

Fig. 12. Examples of polarization measurements with the analyzer. Plotted is the intensity of the laser light versus the orientation of the Glan prism. For the broken curve $S_{\text{lin}} = 0.94 \pm 0.004$ and $\phi_{\text{lin}} = 114.2° \pm 0.2°$; for the solid curve $S_{\text{lin}} = 0.085 \pm 0.002$ and $\phi_{\text{lin}} = 148.4° \pm 0.8°$.

To minimize the degradation of the polarization during the transport to the IP by reflections off mirrors (due to unequal reflectivities and phase shifts of the p and s components [24]), vertically and horizontally polarized light are transported to mirror M4 and are converted to circularly polarized light before entering the machine vacuum by a $\lambda/4$ plate located in front of the window.

The performance of a Pockels cell is very sensitive to its alignment in a laser beam and to the beam quality. Birefringence is induced in the crystal by applying a longitudinal voltage. If the laser light does not enter the crystal perpendicularly to the optic axis, changes in the applied voltage can produce shifts of the beam exiting the crystal. Small angular shifts can result in large shifts of the laser beam position at the IP. The effects of nonuniformities in the crystal and in the voltage across it are minimized when the laser beam is narrow and well collimated.

The polarization of the laser light is monitored with a computer controlled analyzer located after the exit window of the vacuum chamber. A rotating Glan polarizing prism is utilized, and the intensity of the light passing through the polarizer is measured as a function of the angle ϕ of the polarizer. A fit of the intensity is made to the function

$$I(\phi) = I_0 + J \cos 2(\phi - \phi_{\text{lin}}). \tag{41}$$

[#3] Model AOM130M-6.

The degree of linear polarization can be calculated from the maxima and minima of $I(\phi)$:

$$S_{\rm lin} = \frac{I_{\rm max} - I_{\rm min}}{I_{\rm max} + I_{\rm min}} = \frac{J}{I_0} \tag{42}$$

and the orientation (the direction of maximum intensity) is $\phi_{\rm lin}$. Examples of measurements with the analyzer are shown in fig. 12, together with the values obtained for $S_{\rm lin}$ and $\phi_{\rm lin}$.

The Stokes components $S_1(0)$ and S_3 are needed for calculations of the Compton cross section. The calculation of $S_1(0)$ from $S_{\rm lin}$ and $\phi_{\rm lin}$ is performed using eq. (14). The magnitude of S_3 is obtained using eq. (11), but with the present design of the analyzer its sign is not measured. The phase shifts of the components in the transfer line have been measured and the sign deduced from the net phase shift, following the convention that $S_3 > 0$ corresponds to left handed helicity, and $S_3 < 0$ to right.

With the accurate measurements of the linear component of the laser light it is possible to perform a detailed comparison of the measured and predicted asymmetry distributions of the backscattered photons. ΔS_1 can be measured with the analyzer and independently by fitting the measured vertical asymmetry distribution to eq. (37). The comparison may be difficult because the photon polarization is not measured directly at the IP but in the optical lab and with the analyzer located behind the exit window. Measurements of the light polarization before and after the beam has passed through the vacuum chamber and the results of the fits of the backscattered asymmetry distributions (section 5.4.1) indicate that the entrance window of the electron vacuum chamber changes the polarization slightly but the exit window does not. The analyzer then measures the polarization state of the laser beam at the IP.

3.2.3. Luminosity

The average number of backscattered photons produced in an interaction of an electron bunch with the laser beam can be written

$$N = I_{\sigma_c} \mathscr{L}, \tag{43}$$

where σ_c is the total Compton cross section, I is the bunch current and $\mathscr{L}$ is the luminosity of the interaction. For our case of a continuous laser beam crossing the bunched electron beam with a small vertical crossing angle, the luminosity per bunch pass, $\mathscr{L}$, can be written [29]:

$$\mathscr{L} = \sqrt{\frac{2}{\pi}} \frac{n_e \lambda_\gamma}{\alpha} \frac{1}{\sqrt{\sigma_{e,x}^2(0) + \sigma_\gamma^2}}, \tag{44}$$

where it has been assumed for the derivation that the beams lie in a vertical plane and their cross sections

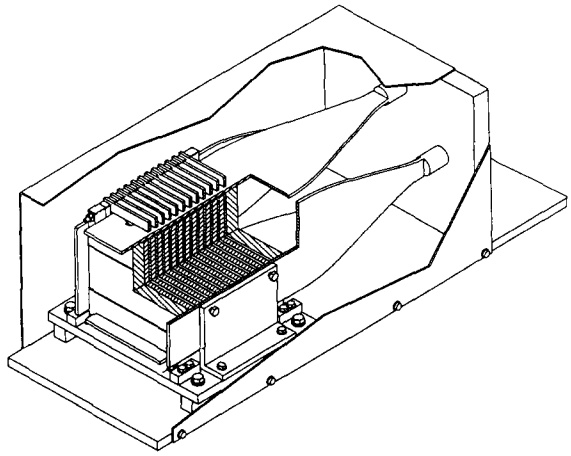

Fig. 13. A cutaway, perspective view of the calorimeter. One can see the sampling layer structure and the U and R wavelength shifters.

are Gaussian. $\sigma_{e,x}(0)$ and σ_γ are the horizontal widths of the electron and laser beams at the IP, α is the vertical crossing angle, n_e is the number of electrons in the bunch (1.32×10^{11} mA^{-1}), and λ_γ is the linear density of photons in the laser beam (at 10 W, $\lambda_\gamma = 8.6 \times 10^8$ cm^{-1}). The beam widths are $\sigma_{e,x}(0) = 0.77$ mm and $\sigma_\gamma \approx 0.6$ mm. The maximum luminosity $\mathscr{L}$ is then 3.0×10^{23} cm^{-2} mA^{-1}. The average number of backscattered photons per bunch pass is then 0.11 mA^{-1}. With the design current of the machine (60 mA in 210 bunches) the average backscattering rate is 300 kHz which exceeds the design rate by a factor of 3.

3.3. The calorimeter

The detector must measure the energy and the vertical position of high energy photons. The photon detector is a sampling calorimeter with 12 layers of tungsten (6.2 mm DENSIMET17, 1.6 X_0) and scintillator (2.6 mm SCSN-38); see fig. 13. The design was chosen for its simplicity in construction, calibration, and the small number of readout channels which it uses. The optical components and materials (e.g., scintillator, wavelength shifters (WLS), and photomultiplier tubes (PMT)) are identical to components used in the ZEUS calorimeter [3]. Each layer consists of a single absorber plate and two optically decoupled scintillator plates. Conceptually, it can be considered to consist of two calorimeters, one on top of the other. The tungsten plates are 60×55 mm^2 and are set in lead frames of 120×100 mm^2 to aid in the alignment of the detector in the beam. The scintillation light from each half is collected with wavelength shifters along the top and bottom of the detector (channels U and D). The vertical position measurement is made by comparing the energy measured in the two channels.

For calibration and redundancy, there are also WLSs on the right and left sides which read the upper and lower halves together (channels R and L). Photomultiplier tubes (Hamamatsu R580) transform the light from the WLSs into an electrical signal. The voltages of the individual electrodes of the PMTs are generated by Cockcroft–Walton bases which deliver constant cathode and dynode voltages up to anode currents of 40 μA. A LED pulser has been used to verify that the PMT gains are stable within ±1% up to frequencies of 400 kHz [30]. The calorimeter response has been simulated [31] using the Monte Carlo program EGS4 [37].

3.3.1. Energy measurement

The measurement of photon energy is made summing two halves of the calorimeter: the "vertical" energy E_V is $E_U + E_D$ and the "horizontal" energy E_H is $E_L + E_R$. Summing improves the uniformity of the energy measurement over the central region and reduces the fluctuations due to photoelectron statistics. The sampling fraction of the calorimeter for electromagnetic showers (the energy deposited in the scintillator divided by the total incident energy) is 2.5% for high energy photons. The efficiency of the calorimeter is small for measuring low energy photons (as the first tungsten plate absorbs the photon energy). We will use the simple approximation that the energy dependence of the sampling fraction can be described using an energy cutoff E_{cut}: for photons of energy below E_{cut} the sampling fraction is zero, and above E_{cut} the value takes the high energy limit. Based on the Monte Carlo simulations we estimate that E_{cut} is approximately 1 MeV.

The sampling fraction for showers developing inside the lead frames is 1.5 times bigger than in the central tungsten plates. This feature is used to position the scattered photon beam on the geometric center of the calorimeter by locating the edges of the tungsten plates using the backscattered photons.

The energy resolution and uniformity have been measured in test beams at DESY and at CERN [32,33]. The uniformity is within ±1% over the central region. The measured energy resolution $\sigma/\langle E\rangle = 24\%/\sqrt{E(\mathrm{GeV})}$ is in agreement with the Monte Carlo simulations. A small (2% at 20 GeV) nonlinearity is present in the energy scale. The measured efficiency of production and collection of scintillation light produced in electromagnetic showers is about 200 photoelectrons per GeV of incident energy. The gains of the PMTs are set to 6.25 picocoulombs per incident GeV.

3.3.2. Position measurement

The vertical position y of a high energy photon is deduced from the asymmetry η_V of the measured vertical energy

$$\eta_V = \frac{E_U - E_D}{E_U + E_D}. \tag{45}$$

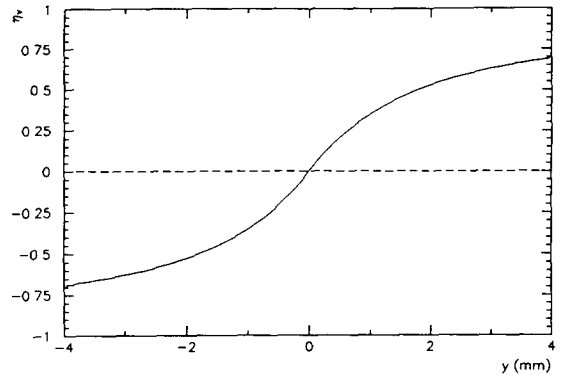

Fig. 14. The transformation function $\eta_V(y)$.

Using a parametrization of the electromagnetic transverse shower shape of the form

$$\frac{dE}{dy}(y) \propto \frac{C_1}{2\lambda_1} e^{-|y|/\lambda_1} + \frac{1-C_1}{2\lambda_2} e^{-|y|/\lambda_2} \tag{46}$$

one can derive the following expression for η_V as a function of the vertical position y of the photon:

$$\eta_V(y) = 1 - \left[C_1 e^{-|y|/\lambda_1} + (1-C_1) e^{-|y|/\lambda_2}\right]. \tag{47}$$

Measurements have been made in a DESY test beam with 1 and 3 GeV electrons [32] and the best-fit values found for the parameters are $C_1 = 0.486 \pm 0.056$, $\lambda_1 = 1.14 \pm 0.05$ mm, and $\lambda_2 = 7.14 \pm 0.51$ mm. This function is shown in fig. 14. The parameters are only weakly dependent on the incident energy. In what follows we shall use the measured variable η_V, and the vertical distributions described in section 2 will be transformed from y to η_V using the above transformation.

The position resolution σ_y is expected to scale as $1/\sqrt{E_\gamma}$ and is approximately a linear function of the vertical position with respect to the split between the upper and lower halves. At 3 GeV a position resolution $\sigma_y = 0.5$ mm was measured for photons hitting the center of the calorimeter, and the resolution is expected to be about 0.3 mm at 10 GeV. (This is of the same order as the smearing $\sigma_{e,y}(65)$ due to the electron beam divergence.) The measurements are in agreement with the Monte Carlo simulations. A simple parametrization has been used to describe the position resolution as a function of vertical position and incident energy:

$$\sigma_{\eta_V}(\eta_V, E_\gamma) = \sqrt{\frac{1-\eta_V^2}{N_P E_\gamma}}. \tag{48}$$

The best fit for the parameter N_P from comparisons with measurements and the Monte Carlo results is 10 GeV^{-1}.

The calorimeter has been carefully aligned in the HERA tunnel, and the plane separating the two calorimeter halves is parallel to the machine plane within ± 4.3 mrad. The calorimeter is placed on a table which is remotely adjustable horizontally and vertically with step sizes of 0.2 μm. The mean vertical position of the Compton photons is monitored and the table is adjusted to keep the beam centered on the calorimeter within ± 50 μm.

3.3.3. Calibration

The on-line calibration of the calorimeter is made by adjusting the voltages of the four PMTs, and the optimal settings are found in a sequence of measurements [30]. With the detector centered in the backscattered beam, the calibration of channels L and R is done first. The absolute calibration of the horizontal energy (GeV/ADC channel) is set using the characteristic edge of the Compton energy spectrum, 13.2 GeV (see fig. 21, section 5.3). The relative calibration of the two channels is done by measuring the distribution of the asymmetry of the horizontal energy η_H:

$$\eta_H = \frac{E_L - E_R}{E_L + E_R}. \tag{49}$$

The distribution is approximately Gaussian, and the width is determined by photoelectron statistics. When the two channels are properly calibrated the mean is zero. Using this method the relative horizontal calibration can be set to an accuracy of 0.1%.

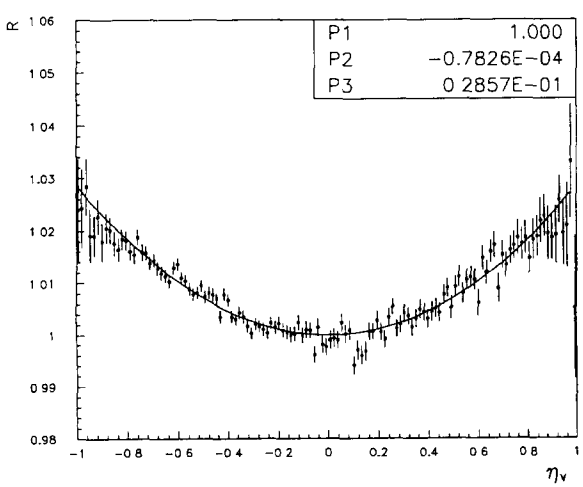

Fig. 15. The calorimeter energy ratio R plotted as a function of η_V. Also shown is a fit to the parabola $R(\eta_V) = P_1 + P_2\eta_V + P_3\eta_V^2$. Properly calibrated, the curve is symmetric in η_V and $R(0) = 1$ (i.e. $P_1 = 1$ and $P_2 = 0$). The quadratic term is small (note the vertical scale); $P_3 \approx 0.03$.

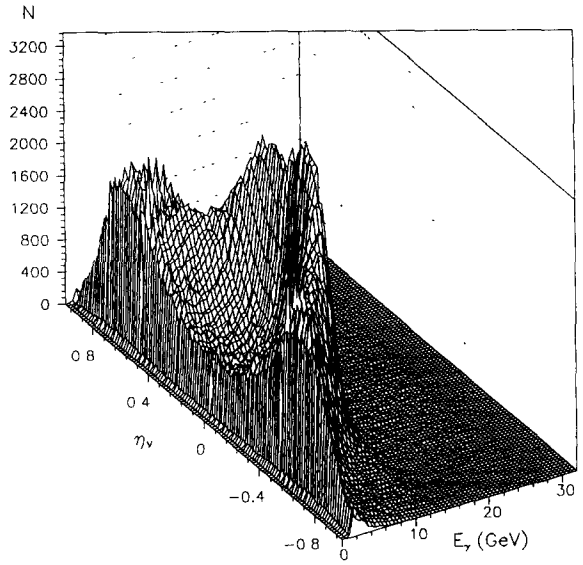

Fig. 16. An example two-dimensional histogram collected with the Digital Card. Plotted is the number of events versus the energy (the width of one energy bin is approximately 0.5 GeV) and the vertical position η_V. Note the narrowing of the vertical distribution with increasing energy, and the sharp drop in the spectrum at the kinematic limit (13.2 GeV). The mean position of the beam-gas bremsstrahlung photons (which dominate at low energies) is seen to be above the mean position of the backscattered photons. The measurement of the Compton scattering energy and vertical position spectra are discussed in sections 5.3 and 5.4.

The vertical channels are calibrated utilizing the calibrated horizontal channels through the energy ratio [33]

$$R(\eta_V) = \frac{E_V}{E_H} = \frac{E_U + E_D}{E_L + E_R}. \tag{50}$$

As horizontal and vertical readout channels view the same scintillators, this ratio, apart from minor effects due to the light attenuation in the scintillator, is independent of position and energy if the relative calibration of U and D is properly set. The absolute vertical calibration is set with the requirement that at the center ($\eta_V = 0$) $R = 1$. The statistical fluctuations of this ratio are small, limited only by the fluctuations due to photoelectron statistics. The ratio is plotted as a function of η_V in fig. 15. With these measurements the relative vertical calibration is easily set to an accuracy of 0.2%.

The calorimeter calibration can be checked without beam with a pulsed LED. Checks of the calibration were made with beam approximately once per day. The pedestals, with widths of about 2 ADC channels, varied

within ± 0.3 channel during the run period. The day-to-day stability of the calorimeter calibration was 0.5%.

3.4. Data acquisition

The data acquisition (DAQ) system has to satisfy the following requirements:
- digitization of four analog channels with 12 bit accuracy,
- average trigger rates up to 100 kHz,
- switching of the photon polarization at 90 Hz,
- measurement of background,
- prompt on-line results for feedback during optimization of the electron polarization, and
- recording of data for off-line analysis.

A typical run sequence for polarization measurements is 40 s of Compton scattering measurements, switching at 90 Hz between left and right circularly polarized light followed by 20 s of background measurements, with the laser beam blocked by the chopper. At the design trigger rate the calorimeter data flow is about 800 kbyte/s. To avoid the storage of large data sets, multi-dimensional histograms are accumulated instead of N-tuples corresponding to individual events. Histograms of event number versus E_γ and η_γ (64×128 bins) for each polarization state and for the background are accumulated. An example histogram is shown in fig. 16. Several one-dimensional histograms are also collected to monitor the calorimeter calibration. In this way the 48 Mbyte needed to store the N-tuples from a 1 min run is reduced to three histograms requiring only 100 kbyte. In addition the data are readily available for on-line and off-line analysis.

The hardware used includes the Digital Card of the ZEUS calorimeter readout [35], a VME based module with four 1 MHz 12 bit ADCs, a highly parallel digital signal processor (Motorola 56001 DSP) with 100 ns instruction time and 120 kbyte of memory. Programs are run on the DSP which do the necessary pedestal subtractions and gain corrections and which accumulate the desired histograms of the data. Programs have been written which produce histograms for pedestal calculations, calibration, the measurement of energy spectra, and which calculate the two-dimensional histograms for the polarization measurement. The completed histograms are readout from the VME module under the control of the equipment computer.

Fast electronics process the signals from the photomultiplier tubes and generate the DAQ trigger. The steering of all devices and the acquisition of data are controlled by a DEC μVAX-III and a DEC-Station 3100. An overview of the various components of the DAQ system is shown in fig. 17 and is described in the following subsections; more details can be found in [34].

3.4.1. The fast electronics

Aircore cables (HF-ALKOAX 4.0/11.5-Philips AG) are used to bring the photomultiplier signals to the West Hall for processing. The total distance is about 250 m. The attenuation of the cable is 0.008 dB/m and

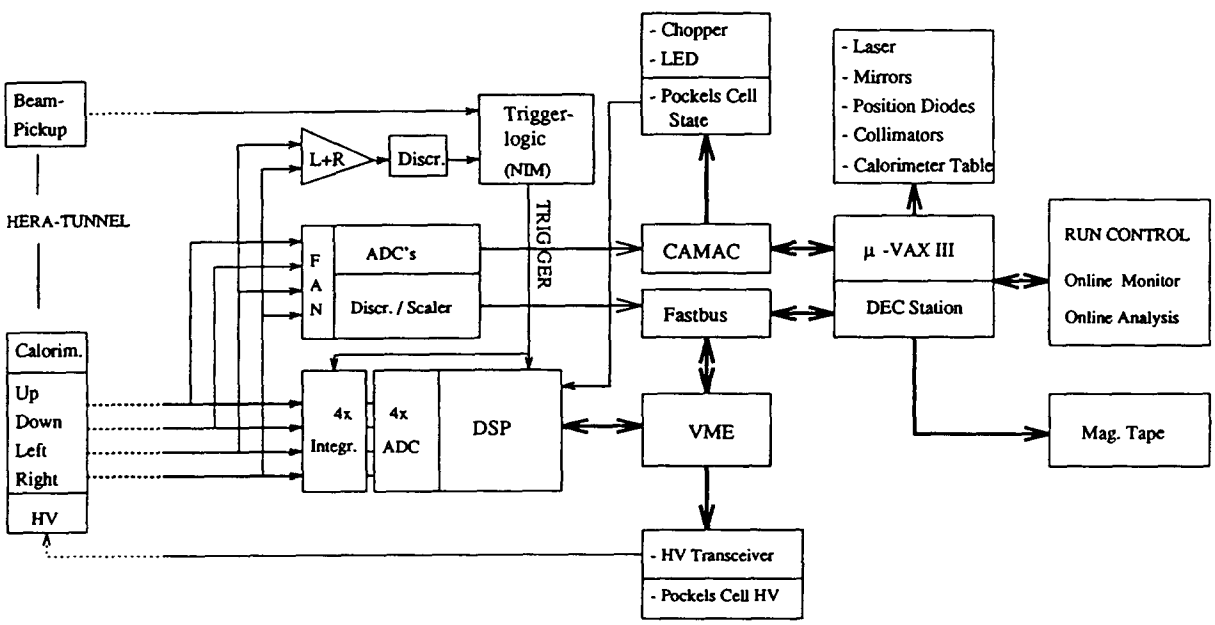

Fig. 17. An overview of the polarimeter DAQ system.

the capacitance is 85 pF/m. The pickup and grounding noise was less than 1 mV.

In the West Hall the signals are fanned-out for generating the trigger and for measurements with the ZEUS Digital Card. To split the signals with minimal distortion the signals for the measurement with the Digital Card are on 50 Ω lines and the samples are derived via high impedance couplings. The couplings are dc to avoid pile-up effects at high rates. To complement the histograms of the Digital Card, the samples are measured with CAMAC analog-to-digital converters (ADCs) triggered at a prescaled rate.

At low photon energies the photon spectrum is dominated by background. Therefore the Compton scattering data are most efficiently collected with an energy threshold on the trigger. The threshold is set by adding the L and R channels (forming the horizontal energy) and setting a voltage threshold on the analog sum. A minimum voltage of 30 mV corresponds to an energy cut of 1.75 GeV. A bunch signal derived from the output of an electron beam position monitor is put in coincidence with the L + R discriminator signal to set the timing of the energy trigger. For measurements down to zero energy the bunch signal alone is used as trigger.

The calorimeter signals are measured by integrating the total charge in the PMT pulses. Integrators, gated by the trigger, integrate each channel for 100 ns and produce a flat-top voltage proportional to the total charge. The voltages are sampled by the ADCs on the Digital Card. The trigger is blocked for the 2 μs needed for the ADC conversion and for baseline restoration. The digitized values are loaded into a dual-port memory which is accessible by the DSP. The events are loaded into a FIFO (64 events deep) and so, although the average trigger rate is limited to about 100 kHz by the time needed for the DSP calculations, peak rates up to 500 kHz are achievable without dead time.

The helicity state of the laser light is encoded and sets a level in the Digital Card. The DSP tests the bit and is thus able to accumulate separate histograms for each state.

FASTBUS scalers are used to monitor the trigger rates for each polarization state and the background.

3.4.2. The on-line control system

In addition to the Digital Card and the trigger, the on-line control system steers the following devices:
- the laser,
- the mirrors M2 and M3,
- the PSDs behind mirrors M3 and M4,
- the polarization analyzer which includes a stepping motor for the Glan prism and a PSD,
- the vertical and horizontal collimators,
- the calorimeter table,
- the voltage controller for the PMT bases, and
- the laser beam chopper.

The first six items are controlled from the μVAX-III via RS-232 serial links. To minimize the noise picked-up on the PMT base voltages the settings are encoded and sent digitally to the detector by a VME module in the West Hall. A receiver next to the calorimeter decodes the information and generates the desired voltages for the bases. Monitor voltages are digitized and sent to the West Hall for monitoring. The laser beam chopper is controlled via CAMAC.

The histograms produced by the Digital Card and the status of all devices are collected by an event-builder and written onto magnetic tape. Information is collected from the data stream by the on-line task which calculates intermediate results which are displayed for the operators.

4. Run conditions and data collected

The first measurements of Compton scattering were made in July 1991. With the data from those measurements the optical system was completed and the on-line system was improved. Parasitic measuring time was used for setting-up and monitoring the performance of the polarimeter. During this time the calibrations of the calorimeter, alignment of the laser beam, adjustments of the Pockels cell voltages and optimization of the polarization of the laser light, and scans with the collimators were performed. The electron polarization measurements reported here were made during dedicated shifts on the 18th and 19th of November 1991.

During the measurements there were typically four bunches in the machine with the total current between 1 and 2 mA. The vacuum pressure at the IP was approximately 2×10^{-9} mbar. The laser was operated at 10 W. At a current of 1.2 mA of 26.6 GeV electrons the background rate (above the threshold of 1.75 GeV) was about 600 Hz and with the laser on the trigger rate was 4 kHz. The laser beam was blocked with the chopper for 20 s of each minute to measure the background. A single polarization run lasted typically 10 min during which 1.6×10^6 backscattered photons were collected. The operating voltages of the Pockels cell were set to optimize the left and right circular polarization states of the laser light at the IP. The polarization at each setting was regularly monitored and the Pockels cell voltages were adjusted if drifts were observed. The linear components of the two helicities were between 0.10 and 0.15, and $\Delta S_1 < 0.04$ with $\Delta S_3 > 0.99$. The helicity of the light was switched between left and right at a rate of 90 Hz. The calibration of the calorimeter was regularly checked and was maintained to better than 1%.

Important parameters were continuously measured

and displayed to monitor the performance of the polarimeter and the progress of the measurement. The vertical electron polarization was available on-line to guide the operators of the electron ring during optimization of the polarization. Trigger rates with both the laser on and blocked were used to monitor the luminosity and the bremsstrahlung background; adjustments of the mirror M3 were made when the luminosity dropped due to motion of the electron or laser beams. The mean vertical position of the backscattered photons at the calorimeter was displayed; the position was kept centered on the calorimeter to an accuracy of ± 50 μm by moving the calorimeter table.

The electron ring was operated with the standard optic which was also used in July 1991. The orbit was well corrected and the rms deviation of the vertical closed orbit was $\sigma_{vco} \approx 0.7$ mm. The expected rms misalignment of the quadrupoles is about 0.3 mm, consistent with beam orbit measurements. Based on analysis of the closed orbit, it was estimated that as many as 26 quadrupoles were misaligned by greater than 0.5 mm. The horizontal and vertical betatron tunes Q_x and Q_y were 47.22 and 47.35, respectively. With the nominal amplitude of the accelerating voltage of 132 MV the measured synchrotron frequency f_s was 3.25 kHz, corresponding to a synchrotron tune Q_s of 0.069. The proton machine was not operated during the measurements and the ZEUS and H1 solenoids were not powered. During the July run a coupling of the horizontal and vertical betatron motions was found, which resulted in a rotation, or a tilt, of the cross section of the electron beam ellipse. At the IP the tilt was ≈ 120 mrad. The cause of this coupling is not yet known. Studies indicate that the source of the coupling is distributed along the circumference of the ring. The effect may be caused by distortions of the stray fields of the electron magnets produced by the magnets of the proton ring, which is located above the electron ring. The tilt could be removed with a closed orbit bump located in one octant of the ring. This "decoupling bump" increased the rms vertical closed orbit σ_{vco} to about 1.5 mm. This effect of the correction will be reduced in the future by distributing the bump around the ring. The coupling is expected to reduce the polarization but measurements were made both with and without the decoupling bump because it was not certain if the correction would reduce the polarization further.

Measurements were made around the beam energy of 26.66 GeV, where the tune is centered between two integer spin resonances ($\nu = 60.5$). The polarization is expected to reach a local maximum at this energy and fall to zero to the sides. Two energy scans were performed, and various methods were tried to depolarize the beam. Closed orbit corrections to improve the polarization had been prepared but with the limited time only a few measurements were possible. The details of the measurements and the results are discussed in section 6. In the following section the methods used to analyze the data are discussed and the errors are estimated.

5. Data analysis

5.1. Background

Sources of background photons produced by the electron beam are the synchrotron radiation originating in the weak dipoles, Compton scattering off thermal photons and bremsstrahlung off gas molecules. The interactions of the backscattered photons in the exit window, in the air between the IP and the detector, and in the collimators also contribute to the back-

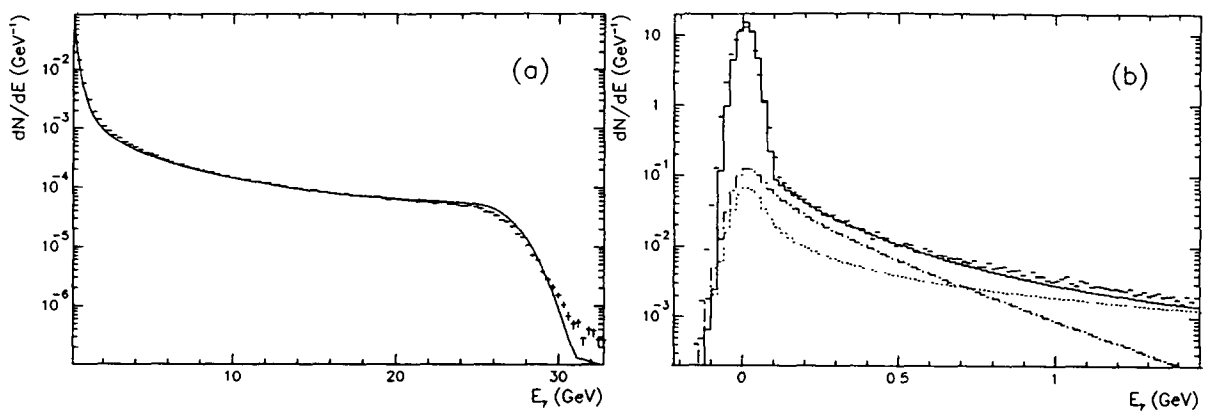

Fig. 18. The background energy spectrum measured with channel L at a beam energy of 26.5 GeV. In figure (b) is shown the low energy region with finer binning. Overlaid (solid curve) is the result of a fit with bremsstrahlung (dotted curve) and Compton-thermal photon (dashed curve) spectra. The fit indicates a vacuum pressure of 1.6×10^{-9} mbar and a temperature of 350 K.

ground. Sweeping magnets which had been installed to study these effects were not operative. For future runs the path to the detector will be evacuated.

5.1.1. Synchrotron radiation

An electron bunch produces many synchrotron photons in each pass through the detector aperture, and statistical fluctuations in the energy deposited in the calorimeter are very small. The expected effect of synchrotron radiation in the calorimeter is then a shift of the zero of the measured energy spectra. At 26.7 GeV the radiation from the weak dipoles has a critical energy of 13 keV and is almost completely absorbed in the first tungsten plate of the calorimeter. The synchrotron radiation has been measured in a previous run with the same calorimeter with the first absorber plate removed [27]. The measured energy shifts were as expected from the radiation produced in the weak dipoles. In the recent measurements very small shifts of each PMT energy spectrum were again found. The shifts, less than 10 ADC channels, do not appear to be due to synchrotron radiation because the shifts normalized to the bunch current were approximately equal at 12 and 26.5 GeV, whereas the energy deposited by synchrotron radiation is a strong function of the beam energy. We believe that these shifts are the result of pickup when the electron machine is running. The shifts were subtracted for the study of the energy spectra but were not subtracted by the DSP in the calculations of η_V. The result is that the transformation function $\eta_V(y)$ is modified slightly producing a small asymmetry in y. The source of the shifts will be studied in more detail during future measurements.

5.1.2. Energy distributions

The energy spectrum of the background at a beam energy of 26.5 GeV is shown in fig. 18. Similar measurements were made at a beam energy of 12 GeV. The spectrum was measured with an energy binning of 15 MeV per channel, and one histogram for each PMT channel was recorded. The pedestals have been subtracted. At energies below ≈ 0.7 GeV the spectrum is dominated by Compton-thermal photons, i.e. photons produced in the Compton scattering of the beam electrons off photons from black-body radiation in the beam pipe [38]. The bremsstrahlung spectrum has been described by the bremsstrahlung cross section in the high energy limit [36] and the Compton-thermal photon spectrum is described by the Planck black body spectrum with the assumption that the spatial distribution of the photons in the vacuum chamber is uniform [30]. A fit has been performed of the measured energy spectra to the sum of the bremsstrahlung and Compton-thermal photon spectra [27]. The parameters of the fit are the average number of bremsstrahlung and Compton-thermal photons N_B and N_{CT} with energy above the calorimeter cutoff energy E_{cut} produced in a single bunch pass. Single- and double-photon spectra are calculated and summed with the Poisson weights determined by the averages. The result of the fit is shown in fig. 18. The results are $N_{CT} = 0.071$ mA^{-1} and $N_B = 0.073$ mA^{-1}. A systematic error can be seen in the fit to the bremsstrahlung spectrum, with the low energy region (below ≈ 6 GeV) underestimated by the theoretical curve and the high energy region overestimated. This is due to the conversion of photons between the IP and the detector. The electrons and positrons produced are multiply scattered and may scatter out of the detector aperture, reducing the measured energy. The probability of conversion is 10%. This has only a small effect on the determination of N_B but will result in an overestimate of the average number of Compton-thermal photons N_{CT}.

The bremsstrahlung rate is proportional to the path of the electrons in units of radiation lengths which is in the calorimeter aperture (including the straight section and the ends of the weak bending magnets, approximately 7 m). The bremsstrahlung fit indicates a path of 3.5×10^{-14} radiation lengths, therefore the average vacuum pressure in the region is 1.6×10^{-9} mbar (N_2 equivalent). The average number of Compton-thermal photons indicates a temperature of 350 K. More precise measurements of the thermal photon scattering will be possible when the photon path to the detector is evacuated. The contribution of Compton-thermal photons is negligible above the 1.75 GeV threshold of the energy trigger.

5.1.3. Vertical distributions

The vertical distribution of bremsstrahlung is approximately energy independent. The rms width of the vertical distribution is $\approx \gamma^{-1}$ and the distribution has long tails. This background dilutes the vertical asymmetries of the polarization measurement. The spectrum is monitored during the measurements so that this background can be accurately subtracted.

Another source of background is the conversion of the Compton photons in the vacuum window (0.5 mm aluminum) and in the 45 m of air between the window and the detector. The multiple scattering of the conversion electrons (few mrad compared to ≈ 20 μrad for the Compton kinematics) results in a flat angular distribution. This background also dilutes the asymmetry in the polarization measurement and because fo the added tails the measured vertical asymmetry distributions in a given energy interval do not fall sharply to zero at the maximum value of y (as shown in fig. 5) but go smoothly to zero. Approximate function forms for the multiple scattering as a functional of energy [39] have been used to estimate the vertical distributions.

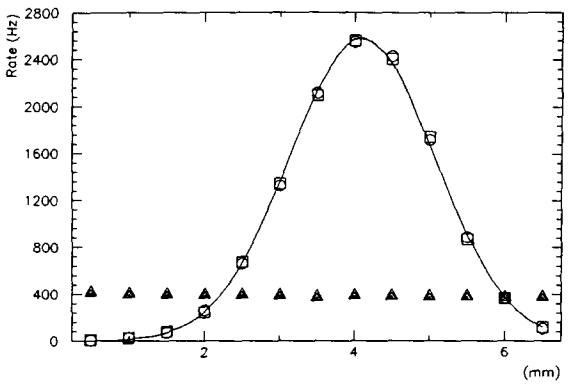

Fig. 19. A scan of mirror M3, showing the Compton scattering rates measured with left (circles) and right (squares) circularly polarized light plotted as functions of the position of the laser beam at the IP (arbitrary zero). The rms widths are 1.0 mm and the difference in the mean positions is 2 ± 8 μm. The background rate at each point (triangles) is shown for reference.

5.2. The electron–photon interaction point

The laser beam crosses the electron beam from above with a vertical crossing angle of 3.1 mrad. The positioning of the laser beam with respect to the electron beam is done with the mirror M3, which is adjustable around both vertical and horizontal axes. It is positioned 18 m from the IP. Rotation of M3 about its vertical axis sweeps the laser beam horizontally which changes the electron-laser luminosity. Rotation about the horizontal axis moves the IP longitudinally.

5.2.1. Luminosity

The maximum luminosity is achieved when the laser beam crosses through the center of the electron beam. The backscattering rate can be written using eq. (43) as a function of the horizontal distance between the centers of the two beams (Δx):

$$\frac{\mathrm{d}N}{\mathrm{d}t}(\Delta x) = I\sigma_{\mathrm{c}} f_{\mathrm{B}} \mathscr{L}(\Delta x), \tag{51}$$

where f_{B} is the bunch revolution frequency (47.4 kHz), I is the total electron beam current,

$$\mathscr{L}(\Delta x) = \mathrm{e}^{-\Delta x^2/2(\sigma_{\mathrm{e},x}^2 + \sigma_\gamma^2)} \mathscr{L}(0), \tag{52}$$

and $\mathscr{L}(0)$ is given by eq. (44). The horizontal position of the laser beam at the IP is adjusted by moving mirror M3 about its vertical axis. The trigger rate is a Gaussian function of the mirror position and the width of the distribution is $\sqrt{\sigma_{\mathrm{e},x}^2 + \sigma_\gamma^2}$; the maximum value is a measure of $\mathscr{L}(0)$.

The results of a scan of mirror M3 is shown in fig. 19, where the backscattering rates for left and right circular polarizations after background subtraction have been plotted versus the position of the laser beam at the IP. The measured luminosity $\mathscr{L}(0)$ corresponds to an average number of backscattered photons per bunch pass of 0.076 mA^{-1} and the measured width $\sqrt{\sigma_{\mathrm{e},x}^2 + \sigma_\gamma^2} = 1.0$ mm is in agreement with our estimates (see section 3.2.3).

5.2.2. Shifting of the laser beam position

If the Pockels cell is poorly aligned then a change in the voltage across the cell can shift the position of the laser beam at the IP. The horizontal shift can be determined from luminosity scans with mirror M3 while switching the polarization state of the laser light. During the measurements in July 1991 the curves measured with left and right circular polarization had a relative offset of approximately 0.32 mm, indicating that the position of the laser beam was polarization dependent. This was corrected by realignment of the Pockels cell together with other improvements in the optical transport system. The curves shown in fig. 19

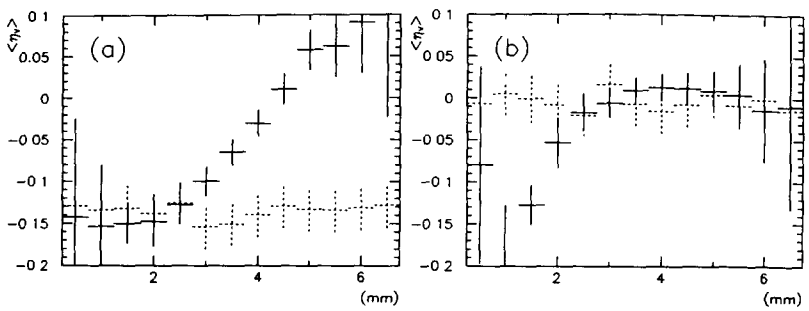

Fig. 20. Two scans of mirror M3 where the mean vertical position η_{V} of the backscattered photons is plotted as a function of the position of the laser beam at the IP. The corresponding scattering rates are plotted in fig. 19. Figure (a) shows a scan made without the decoupling bump. A vertical offset of the backscattered beam of 0.5 mm corresponds to $\eta_{\mathrm{V}} = 0.15$, thus the slope corresponds to 220 mrad. After the first scan was finished, the decoupling bump was added to the machine optics and the detector was moved to center the backscattered photons. A second scan was then made, and the results are plotted in figure (b). The slope at the center of the electron beam is consistent with zero. The bremsstrahlung mean position is also plotted (broken points) for reference.

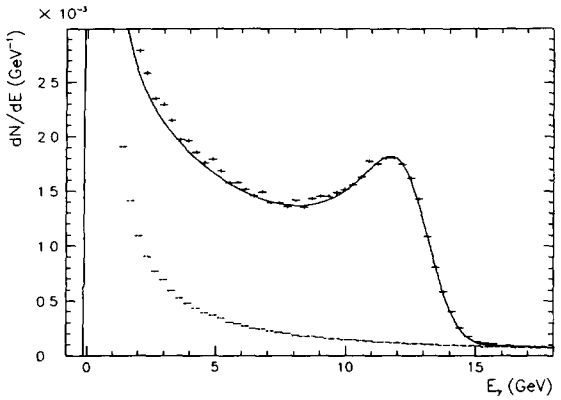

Fig. 21. The energy spectrum measured with a laser power of 10 W. The energy of the electron beam was 26.5 GeV and the current was 0.32 mA. The background is not subtracted. Overlaid is the result of a fit, which indicates an average number of Compton scattered photons per bunch pass of 0.021. The background spectrum is shown for comparison (see fig. 18).

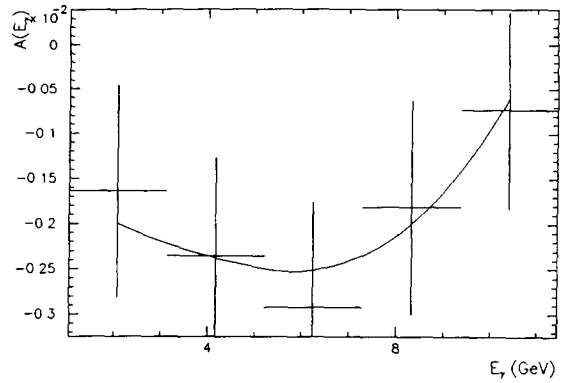

Fig. 22. An example of an energy asymmetry distribution, measured at a beam energy of 26.65 GeV. The asymmetry is plotted as a function of the energy E_γ. Overlaid is a fit to eq. (53) which gives $\Delta S_3 P_Z = 5.6 \pm 4.1 \times 10^{-3}$ and $\mathscr{A}_0 = 1.58 \pm 0.55 \times 10^{-3}$.

have a relative shift of the means of 2 ± 8 μm. Regular checks showed that the relative shift was negligible during the measurement period.

5.2.3. Tilt of the electron beam ellipse

The tilt of the electron beam ellipse found in July can be seen by plotting the mean vertical position of the backscattered photons as a function of the horizontal position of the laser beam at the IP. Fig. 20a shows a scan of the mirror M3 made without the decoupling bump. The slope of the measured curve indicates that the tilt of the electron beam ellipse at the IP was approximately 220 mrad. After the decoupling bump was introduced the scan was repeated and the results are plotted in fig. 20b. The slope in the center of the electron beam is consistent with a tilt of zero. The effectiveness of the decoupling bump was monitored during the measurement period.

5.2.4. Beam steering by the quadrupole

The electron and laser beams overlap over a length of about 50 cm and the longitudinal position of the IP can be changed by rotating M3 about its horizontal axis. Bremsstrahlung photons which reach the detector are produced in the straight section and in the ends of the weak dipoles, a region of approximately 7 m in length. We have found that the mean vertical positions of the Compton-scattered and bremsstrahlung photons are generally not the same, and differ by as much as 0.5 mm. This can be understood if the electron beam is vertically off-center in the quadrupole located in the straight section. The quadrupole then bends the beam vertically and the mean vertical position of the bremsstrahlung photons produced upstream of the quadrupole is different than that of the photons produced downstream. A vertical offset of less than 0.3 mm would produce the measured effects, consistent with the rms vertical closed orbit error of 0.7 mm.

5.3. Compton scattering energy distributions

The measured energy spectrum is shown in fig. 21 for a beam energy of 26.5 GeV. The background spectrum has not been subtracted. The laser power was 10 W. Spectra were measured with left and right circular polarizations and added to cancel the effects of longi-

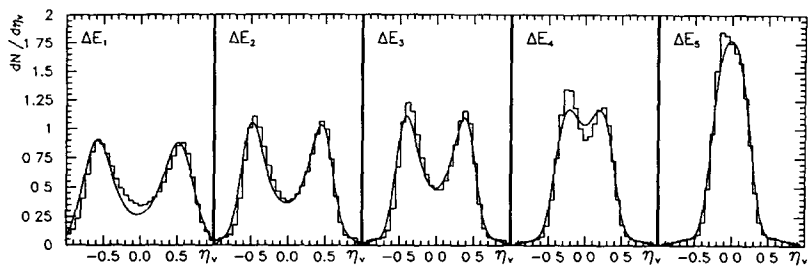

Fig. 23. Measured vertical distributions $dN/d\eta_V(\eta_V)$, plotted versus η_V in the five energy intervals. Overlaid are expected curves calculated from y distributions including a description of the calorimeter response functions.

tudinal electron polarization. The predicted spectrum smeared by the calorimeter energy resolution is also shown, as well as the background spectrum measured with the laser beam blocked. The Compton scattering rate above the threshold of the energy trigger (1.75 GeV) is 70% of the trigger rate and in the energy range from 5.2 to 11.9 GeV the signal-to-background ratio is nearly 10-to-1.

5.3.1. Energy asymmetry distributions

The asymmetry of the energy spectra measured with left and right helicities have been used to measure the longitudinal component of the polarization. The measured energy asymmetry distributions have been fitted to eq. (36) with an additional constant term $\mathscr{A}_0$:

$$\mathscr{A}(E_\gamma) = \frac{N_L(E_\gamma) - N_R(E_\gamma)}{N_L(E_\gamma) + N_R(E_\gamma)} = \Delta S_3 P_Z \Sigma_{2Z/0} + \mathscr{A}_0. \quad (53)$$

The free parameters of the fit are $\Delta S_3 P_Z$ and $\mathscr{A}_0$. The constant term accounts for differences in the total number of photons for each helicity. The two datasets have been normalized for equal time in each photon polarization state. An example distribution together with the results of the fit are shown in fig. 22. The beam energy was 26.65 GeV. The results are $\Delta S_3 P_Z = 5.6 \pm 4.1 \times 10^{-3}$ and $\mathscr{A}_0 = 1.58 \pm 0.55 \times 10^{-3}$. The nonzero value of $\mathscr{A}_0$ is believed to be due to differences in the reflectivities of the mirrors and the transmission of the Pockels cell in the two polarization states, which results in a small polarization dependence of the luminosity $\mathscr{L}$. The calculation of P_Z from $\Delta S_3 P_Z$ is discussed in section 5.5.

5.4. Compton scattering vertical distributions

Examples of vertical distributions measured with the calorimeter are shown in fig. 23. Spectra measured with left and right circular polarizations have been added to cancel polarization effects. The energy dependence is shown by summing the photons in each of the five energy intervals used in section 2 and plotting $dN/d\eta_V(\eta_V)$ for each interval. The background measured with the laser beam blocked has been subtracted. The tails are the result of the multiple scattering of the charged particles produced by converted photons (section 5.1.3).

The predicted distributions are also shown in fig. 23. The calculations include preliminary descriptions of the calorimeter response functions. The transformation of the predicted spectra in y (fig. 4) to the measured variable η_V has been performed with eq. (47) and the calorimeter position resolution has been simulated using eq. (48). The energy cuts used to define the five intervals have been smeared to simulate the energy resolution of the calorimeter. Approximations for the multiple scattering of charged particles have been used to calculate the vertical distribution of the converted photons in order to reproduce the tails.

A comparison of the measured and predicted distributions shows reasonable agreement but systematic errors are present in the simulations. The small asymmetry in η_V is a result of incorrect pedestal subtraction (section 5.1). Measurements of the vertical distributions as functions of E_γ and of the mean position of the backscattered photons on the calorimeter are planned. With these studies we will improve the parametrizations of the calorimeter response functions and the estimate of the projected spot size of the electron beam, $\sigma_{e,y}(65)$. It is possible to separate the smearing of the vertical distributions by the electron beam from the smearing by the detector because the electron smearing is Gaussian in y and is independent of energy, whereas the smearing by the calorimeter is Gaussian in η_V and decreases with increasing energy. The best-fit value of the smearing width $\sigma_{e,y}(65)$ is 0.3 mm, which is within the expected range. Errors in the calorimeter response functions and in the value of $\sigma_{e,y}(65)$ result in errors in the fit functions $\Sigma'_{1/0}$, $\Sigma_{2Y/0}$ and Π. Their influence on the polarization measurement is discussed in section 5.5.1.

5.4.1. Vertical asymmetry distributions

Examples of measured vertical asymmetry distributions $\mathscr{A}(\eta_V)$ are shown in figs. 24–26. The vertical

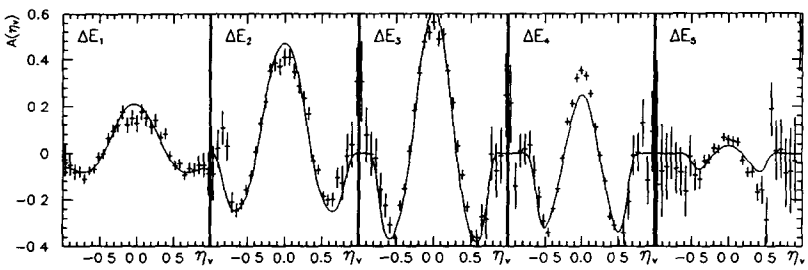

Fig. 24. Asymmetry measurements with vertical and horizontal photon polarizations. The measurement with the analyzer gives $\Delta S_1 = 0.924 \pm 0.006$. The results of the fit are $\Delta S_1 = 0.889 \pm 0.010$ and $\Delta S_3 P_Y = 0.042 \pm 0.024$.

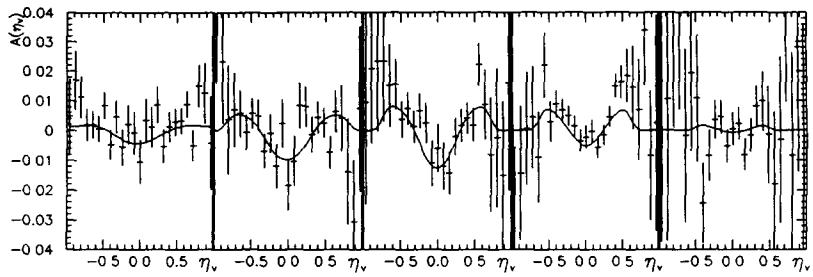

Fig. 25. Asymmetry measurements with circular photon polarizations. The dominant even component of the function indicates that the electron polarization is small. The results of the fit are $\Delta S_1 = -0.0177 \pm 0.0030$ and $\Delta S_3 P_Y = -0.0023 \pm 0.0067$. The measurement with the analyzer gives $\Delta S_1 = -0.0244 \pm 0.0052$.

asymmetry functions $\Sigma'_{1/0}$ and $\Sigma_{2Y/0}$ have been calculated as functions of η_V as described in the previous section. The measured distributions are fitted to eq. (37) with free parameters ΔS_1 and $\Delta S_3 P_Y$ and the results of each fit are shown together with the measurements. The best fit values are found for the five energy intervals simultaneously.

Linear Photon Polarization. One of the best ways to test our understanding of the vertical asymmetry functions is to compare the measured and predicted vertical asymmetry distributions of scattering with vertical and horizontal linear light polarizations. The asymmetry is independent of the polarization of the electron beam: the shape of the asymmetry function $\Sigma'_{1/0}$ is determined by Compton kinematics, the detector response functions and the smearing of the electron beam. The magnitude of ΔS_1 is determined by the polarizations of the laser light used in the measurement. The measured curve obtained in a special run with linearly polarized light is shown in fig. 24 together with the result of the fit. There is good agreement in the shapes of the distributions in the five energy intervals. The results of the fit are $\Delta S_1 = 0.889 \pm 0.010$ and $\Delta S_3 P_Y = 0.042 \pm 0.024$. The value of ΔS_1 measured with the analyzer was 0.924 ± 0.006.

The contribution of linear polarizations to the asymmetries measured with left and right circular polarizations have also been measured. It is more difficult to use these results to check the quality of the fit because the asymmetries are small and the relative statistical errors are large. In fig. 25 we show an example of a vertical asymmetry distribution measured with nearly perfect circular laser light polarizations. The results of the analyzer measurements were $\Delta S_1 = -0.0244 \pm 0.0052$ and $\Delta S_3 = 0.990 \pm 0.006$. The shapes of the measured and predicted distributions are in good agreement but the statistical errors are large. The asymmetry is mostly an even function of η_V indicating that the vertical electron polarization is small and the effect is dominated by the linear components in the laser light. The result of the fit is $\Delta S_1 = -0.0177 \pm 0.0030$ and $\Delta S_3 P_Y = -0.0023 \pm 0.0067$. The correlation of the parameters is 8.2% and the chi-squared per degree of freedom χ^2_{ndf} is 1.4. During the polarization measurements $\Delta S_1 \approx -0.025$ with slow drifts of up to ± 0.015. Checks of the linear polarizations using the analyzer were not made frequently enough to determine the cause of these drifts in the fit results.

The good agreement of the measurements and predictions for the shape and energy dependence of the asymmetry function $\Sigma'_{1/0}$ and the linear polarization parameter ΔS_1 show that the asymmetry distributions are quantitatively well understood, and fitting the asymmetry distribution gives reliable results for the fit parameters.

Vertical Electron Polarization. An example of a measurement with significant vertical electron polarization is shown in fig. 26. The asymmetry is mainly an odd

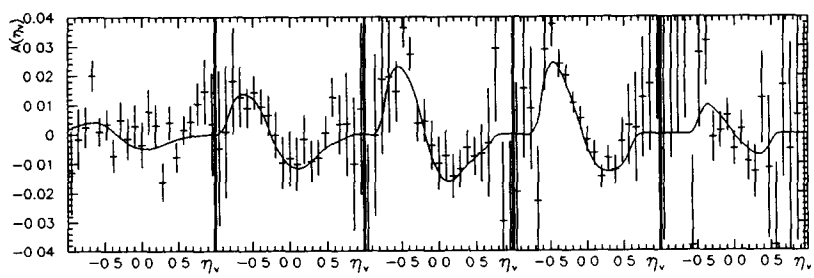

Fig. 26. Asymmetry measurements with circular photon polarizations. The dominant odd component of the function indicates that the electron polarization is the dominant effect. The results of the fit are $\Delta S_1 = -0.0210 \pm 0.0037$ and $\Delta S_3 P_Y = 0.0882 \pm 0.0071$.

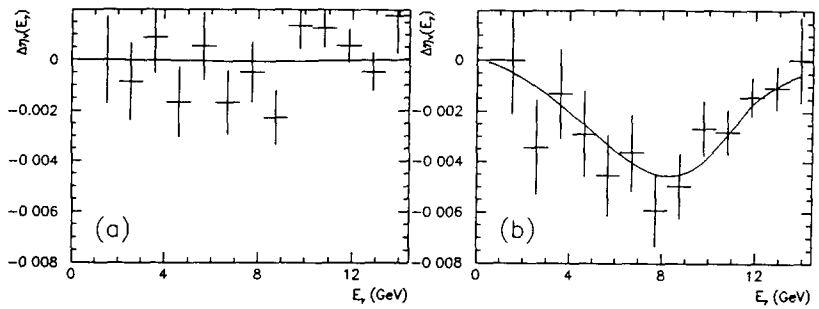

Fig. 27. The mean shift $\Delta\eta_V$ plotted versus the energy E_γ. The data of figures (a) and (b) correspond to the plots shown in figs. 25 and 26, respectively. The results of the fits to eq. (54) are overlaid and the values found for the fit parameter $\Delta S_3 P_Y$ are 0.0014 ± 0.0086 and 0.0800 ± 0.0098.

function of η_V, indicating that the effect of the electron polarization dominates over the effect of the linear polarization in the laser light. The results of the fit are $\Delta S_1 = -0.0210 \pm 0.0037$ and $\Delta S_3 P_Y = 0.0882 \pm 0.0071$. The correlation between the two parameters was 1.2% and the χ^2_{ndf} was 2.1. The predicted shapes are again in good agreement with the measured distributions in the five energy intervals and the result for ΔS_1 is consistent with the result from the analyzer.

5.4.2. Shift of the means

The vertical electron polarization can also be found from measurements of the shift of the means with left and right circular polarizations (eq. (38)):

$$\Delta\eta_V(E_\gamma) = \frac{\langle\eta_V\rangle_L - \langle\eta_V\rangle_R}{2} = \Delta S_3 P_Y \Pi(E_\gamma), \quad (54)$$

where $\Pi(E_\gamma)$ is the shift of the mean position in η_V with $\Delta S_3 P_Y = 1$. The value of $\Delta S_3 P_Y$ is found by fitting the measured mean shift $\Delta\eta_V(E_\gamma)$ to eq. (54). To illustrate this method the results shown in figs. 27a and 27b are calculated from the same data that are shown in figs. 25 and 26, respectively. The results of the fits are $\Delta S_3 P_Y = 0.0014 \pm 0.0086$ and 0.0800 ± 0.0097, in agreement with results of the fits of the vertical asymmetry distributions $\mathscr{A}(\eta_V)$.

Table 1
Summary of the studies of the systematic errors in the scales of the polarization measurements. The maximum errors for each parameter have been quadratically added to estimate the total systematic errors

Input parameter/ Simulated condition	Nominal value	Estimated min. and max. values	Resulting change in polarization scale (%)		
			$\Sigma'_{1/0}$	$\Sigma_{2Y/0}$	$\Pi(E_\gamma)$
$\eta_V(Y)$ transformation					
C_1	0.486	0.430	−2.7	−1.6	7.5
		0.542	1.1	1.6	−6.4
λ_1	1.14	1.09 mm	0.2	0.4	−2.1
		1.19 mm	−0.2	−0.5	2.1
λ_2	7.14	6.63 mm	−0.7	0.3	−1.5
		7.65 mm	0.5	−0.2	1.2
Position resolution N_P	10 GeV^{-1}	4.4 GeV^{-1}	25.8	5.7	0
		22.5 GeV^{-1}	−13.2	−2.3	0
Electron spot size $\sigma_{e,y}(65)$	0.3 mm	0.2 mm	−6.8	−4.2	−1.2
		0.5 mm	19.0	1.1	4.0
Background correction	×1	×0.8	−0.5	0.2	0
		×1.2	0.3	−0.2	0
Calorimeter calibration	1.00	0.98	−0.6	1.5	0.1
		1.02	0.4	−1.6	−0.1
Centering the calorimeter	0 μm	50 μm	0.4	−2.6	0.3
		−50 μm	−0.7	2.4	0.2
Pedestal error	5 ADC ch	0 ADC ch	2.5	−1.5	−1.1
		10 ADC ch	−2.8	1.4	0.9
Total systematic error			32.3	8.0	9.4

To obtain rapid on-line polarization results the mean shift $\Delta\eta_V$ is calculated in a single energy interval where the effect is largest. For the energy interval between 5.2 and 11.9 GeV the analyzing power Π is 0.0456 (142 μm). The shifts $\Delta\eta_V$ in this interval for the two measurements described above yield polarizations $\Delta S_3 P_Y = 0.0003 \pm 0.0065$ and 0.0856 ± 0.0079, which are consistent with the results of the two fitting methods described above.

5.5. Measurement of the electron polarization

The cross section asymmetries which are measured to obtain the vertical and longitudinal components of the electron polarization are proportional to ΔS_3. Although the linear polarization parameter ΔS_1 can be measured by fitting the vertical asymmetry distributions, the value of ΔS_3 can only be found from direct measurements of the polarization of the laser light. During the measurement period we had $0.990 < \Delta S_3 < 0.995$. Assuming a value of ΔS_3 which is too large underestimates the electron polarization; we will use $\Delta S_3 = 1$. Based on the measurements of $\Delta S_3 P_Y$, the sign of the polarization is then positive, as expected from the Sokolov–Ternov effect.

The longitudinal polarization P_Z is measured by fitting the energy asymmetry $\mathscr{A}(E_\gamma)$; the free parameters of the fit are $\Delta S_3 P_Z$ and $\mathscr{A}_0$. The measured values of $|P_Z|$ are small, less than 0.01, with a similar statistical error. The linearity of the calorimeter energy scale is very good, thus the systematic errors in obtaining P_Z by fitting the differential energy spectrum are negligible.

Two methods have been used to extract the vertical polarization P_Y from the Compton scattering measurements: fitting the vertical asymmetry distributions $\mathscr{A}(\eta_V)$ in five energy intervals and fitting the mean shifts $\Delta\eta_V(E_\gamma)$. The statistical errors of the results are less than ± 0.01 with 10^6 backscattered photons per run. The energy dependence of the measured asymmetries, in particular the small effects seen at low and high photon energies, indicates that there is a negligible offset of the polarization scales from zero. This is also seen in the results of the measurements of the horizontal shift of the laser beam and the tilt of the electron beam ellipse which indicate that their combined effect now produces a systematic offset of less than ± 0.001. The polarization scale of the measured asymmetries is sensitive to errors in the fit functions; this is the subject of the next subsection.

5.5.1. Systematic errors in the polarization scale

We have investigated the influence of errors in the fit functions $\Sigma'_{1/0}$, $\Sigma_{2Y/0}$, and Π on the fit results. In addition to the scattering cross section, the input parameters needed to calculate the fit functions include

- the transformation function $\eta_V(y)$ which is parametrized by eq. (47) with parameters C_1, λ_1 and λ_2,
- the calorimeter position resolution $\sigma_{\eta_V}(\eta_V, E_\gamma)$ which is parametrized by eq. (48) with the parameter N_P,
- the spot size of the projected electron beam $\sigma_{e,y}(65)$ which depends on the value of the betatron coupling K.

Uncertainties in these input parameters cause uncertainties in the three fit functions, leading to systematic errors in the measured polarization scales. The calorimeter response functions and the nominal parameter values have been measured in test beams and checked with Monte Carlo calculations. The nominal value of the betatron coupling K, found by fitting the measured vertical distributions, is within the range of expected values. The energy resolution of the calorimeter is also used in the calculations, but its small uncertainty has a negligible effect on the values of the functions. The nominal values of the five parameters are shown in table 1 as well as their possible extreme values. We have estimated the effects of the above uncertainties by using in the analysis fit functions corresponding to the maximum and minimum values of each parameter. Collected in table 1 are the results of using these functions, tabulated as the change in the polarization values compared with the results of the fit with the nominal function. The systematic effects are tabulated for three polarization measurements: measuring the linear polarization term ΔS_1 by means of the function $\Sigma'_{1/0}$; measuring the vertical polarization parameter $\Delta S_3 P_Y$ by means of the function $\Sigma_{2Y/0}$; and measuring $\Delta S_3 P_Y$ by means of the analyzing power Π.

Other sources of systematic errors are approximations in the simulations of the run conditions, for example that the beam is perfectly centered on the calorimeter. The effects studied include the following approximations:

- *Background correction.* High energy background from bremsstrahlung and conversions dilute the asymmetry in the vertical distributions, particularly in the tails where the background dominates. Because the background is sampled often (20 s out of each minute), the measurements are not sensitive to slow time dependent drifts. The background is subtracted from the spectra measured with the laser on, after taking into account the DAQ livetimes of the two measurements. The converted Compton scattered photons cannot be easily subtracted and approximations have been utilized to include them in the predicted distributions. The effects of errors in the background corrections are estimated by comparing the nominal fit results ("×1") with the results when the background is undercorrected by a factor of 0.8 and overcorrected by a factor of 1.2.

- *Calorimeter calibration*. The absolute calibration of the vertical energy $E_U + E_D$ is set using the edge of the backscattered photon spectrum; the error in this calibration is small, and has negligible effects on the measured polarization scale. Errors in the relative calibration of the U and D channels change the effective transformation function $\eta_V(y)$. It is estimated that during the measurements the error in the relative vertical calibration was less than $\pm 2\%$.
- *Centering the calorimeter*. Because of the nonlinearity of the transformation function $\eta_V(y)$, the shape of the asymmetry distributions depends on the mean position of the backscattered photons relative to the calorimeter center. With the scattered beam off-center, the vertical asymmetry functions $\Sigma'_{1/0}$ and $\Sigma_{2\gamma/0}$ are not pure even and odd functions of η_V, which results in a correlation between the components in the fits. The small odd component of the asymmetry with linear light may fake vertical electron polarization in the fit. The linear components of the laser light S_1 were less than 0.15 and the backscattered beam was centered on the table within ± 50 μm.
- *Pedestal errors*. Due to pickup from the electron ring the pedestals subtracted by the DSP in the calculation of η_V were incorrect. This error modifies the effective transformation $\eta_V(y)$ slightly; the dominant effect is from the difference of the errors of the U and D pedestals. The shifts were about four ADC channels in U and nine channels in D. The effect has been estimated with calculations of the new fit functions for relative pedestal errors (D − U) of zero and ten ADC channels.

As seen in table 1, the systematic errors are dominated by the uncertainties in the detector response functions. The predicted distributions for $dN/d\eta_V$ and $\mathscr{A}(\eta_V)$ are in good agreement with the measured histograms, indicating that the transformation and smearing functions are approximately correct. The measurement of the linear polarization is most sensitive to the smearing functions, and thus the good agreement for the values of ΔS_1 from the fits and the analyzer measurements indicates that the nominal values of the smearing parameters have been well selected. The two methods of calculating $\Delta S_3 P_Y$ are sensitive to different errors, and in some cases a parameter variation causes an opposite change of their polarization scales. The polarization results are checked

Table 2
Summary of the polarization results of the November 1991 measurements. The longitudinal component $|P_Z|$ was less than 1%. The maximum vertical polarization measured during the run period was $9.2 \pm 0.8\%$ at 26.67 GeV. The errors shown are statistical

Conditions	Electron beam energy [GeV]	Synchrotron tune Q_s	Vertical polarization [%]
Energy scan from 26.59 to 26.75 GeV			
maxima	26.68	0.069	7.16 ± 0.92
	26.69	0.069	6.89 ± 0.98
synchrotron resonances	26.61	0.069	-0.30 ± 0.89
	26.64	0.069	1.55 ± 1.03
	26.67	0.069	2.29 ± 1.05
	26.70	0.069	-1.18 ± 1.00
	26.73	0.069	0.69 ± 0.91
Effect of the decoupling bump and depolarization by orbit coupling			
no correction	26.65	0.057	0.45 ± 0.69
decoupling bump	26.65	0.057	3.02 ± 0.64
Q_x depolarization	26.65	0.057	-0.37 ± 1.11
no correction	26.67	0.057	4.46 ± 0.62
decoupling bump	26.67	0.057	8.12 ± 0.72
Q_x depolarization	26.67	0.057	0.40 ± 0.77
Depolarization by shifting the Q_s resonances			
nominal conditions	26.67	0.057	9.17 ± 0.79
depolarization	26.67	0.051	3.46 ± 0.86
return to nominal conditions	26.67	0.057	7.89 ± 0.96
depolarization	26.67	0.051	3.04 ± 0.74
return to nominal conditions	26.67	0.057	8.86 ± 0.89

with measurements using both methods, and the results are in agreement within the statistical error of typically ± 0.01.

Owing to low electron currents we were unable to measure the build-up time and so there is no independent check of the scale. Work is continuing to improve the understanding of systematic effects [31]. Based on the studies summarized in table 1 we estimate that the systematic error in the polarization values is below $0.10 P_Y$.

6. Discussion of the results

The results of the November 1991 measurements of the vertical polarization P_Y are summarized in table 2. The horizontal component P_X was not measured. As expected, the longitudinal component P_Z was found to be small; $|P_Z|$ was less than 1%. Representative results from a very long run are $P_Z = 0.56 \pm 0.41\%$ (shown in fig. 22) and $P_Y = 7.3 \pm 0.5\%$. This corresponds to a tilt of the spin vector of 77 ± 57 mrad.

The vertical polarization is expected to reach a maximum value when the spin tune is centered between two integers. The nominal beam energy during the measurements was 26.66 GeV, corresponding to a spin tune ν of 60.5. After evidence of polarization was found, studies of the effects of the decoupling bump and attempts to depolarize were made at 26.65 and 26.67 GeV. The rms vertical closed orbit error σ_{vco} is increased from 0.7 to about 1.5 mm when the decoupling bump is used to remove the tilt of the electron beam ellipse. This additional error increases the tilt of the average spin axis, and thus is expected to strengthen the depolarizing effects. It was found that the polarization increases when the decoupling bump is used: at 26.65 GeV the polarization increased from $0.45 \pm 0.69\%$ to $3.02 \pm 0.64\%$ and at 26.67 GeV from $4.46 \pm 0.62\%$ to $8.12 \pm 0.72\%$. This result can be understood by considering higher-order nonlinear depolarizing effects which seem to be weakened when the tilt is corrected, and thus one can expect that the polarization is left unchanged or even improves by using the decoupling bump.

An important part of substantiating the presence of polarization is to observe the depolarization of the beam and to measure the build-up time of the polarization τ. With a maximum polarization of 10% at 26.7 GeV, the build-up time is only about 5 min and cannot be measured with low beam currents using the single-photon method. Nevertheless, we tried various methods to depolarize the beam, and the first method attempted was to couple the vertical and horizontal betatron motions. The beam is blown up vertically (it becomes round) and the increased horizontal fields experienced by the electrons in the quadrupoles can

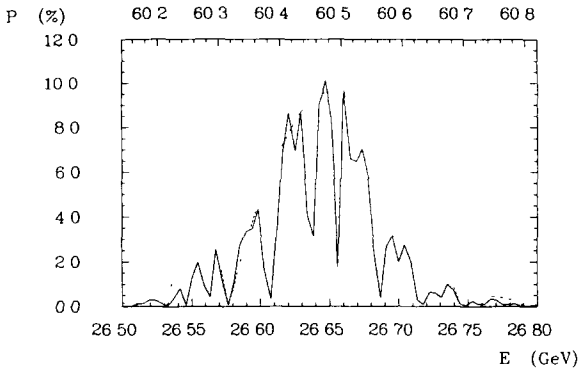

Fig. 28. Theoretical predictions for the polarization as a function of the electron beam energy (lower scale) and of the spin tune ν (upper scale). The maximum polarization is expected at half-integer spin tunes; $\nu = 60.5$ corresponds to a beam energy of 26.66 GeV. The broken curve is the result of the linear calculation. The solid curve is the result of the Monte Carlo tracking calculations, which include the effects of synchrotron sideband resonances.

depolarize the beam. No effect was found when the coupling was made by shifting the vertical tune. A strong effect was found by shifting the horizontal tune: at 26.65 GeV the polarization dropped from $3.02 \pm 0.64\%$ to $-0.37 \pm 1.11\%$ and at 26.67 GeV from $8.12 \pm 0.72\%$ to $0.40 \pm 0.77\%$. The difference in the depolarizing effects of the two methods of coupling may indicate that the dominant depolarizing effect is not the coupling itself, but the result of shifting the positions of higher order resonances.

Simulations have been performed to predict the level of vertical polarization as a function of the beam energy, centered around 26.66 GeV. The results are shown in fig. 28; details about the calculations can be found in [40]. The estimated depolarizing strengths of the resonances are sensitive to the orbit errors and magnet misalignments assumed in the calculations.

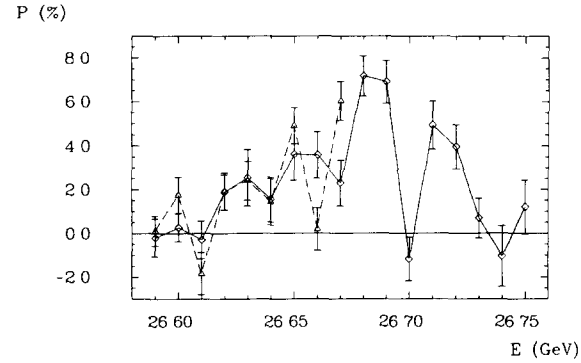

Fig. 29. The results of two scans of the polarization versus the electron beam energy. Both scans were begun at 26.59 GeV and the beam energy was increased in 10 MeV steps.

Thus the predicted maximum polarization has large uncertainties (approximately a factor of 2). The simulations were done with only a single optic with randomly distributed errors which reproduces the measured null (uncorrected) orbit. Two curves are shown: the broken curve is the result of calculations based on analytic theory in which only first order, or linear, depolarizing resonances are treated, i.e. the cases when either m_x, m_y, or m_s equals ± 1 with the others zero; see eq. (5). The solid curve is the result of Monte Carlo tracking simulations in which the full depolarizing effects of higher order resonances are simulated. Comparing the curves, we see that the limits of the envelope of the expected polarization are determined by the positions of the four first order Q_x and Q_y resonances which are located at the energies 26.53 and 26.79 GeV, and 26.57 and 26.75 GeV, respectively. The fine structure seen in the Monte Carlo curve is a result of the depolarizing effects of the synchrotron sideband resonances, possibly of the parent Q_y resonances (i.e. $m_y = \pm 1$ and m_s equals an integer; sidebands up to $m_s = \pm 4$ are visible in the figure). For a synchrotron tune Q_s of 0.069 the spacing of the sidebands is 30 MeV.

Two energy scans were performed during the measurement period and the results are shown in fig. 29. Both scans began at 26.59 GeV and the increment of the beam energy was 10 MeV. The first scan was made without the decoupling bump and extends only to 26.67 GeV. The second scan was made with the decoupling bump and extends to 26.75 GeV. The maximum polarization is 6.68% at 26.68 GeV and the width of the peak is about 50 MeV. Drops in the polarization were found at 26.64, 26.67 and 26.70 GeV.

Shown in fig. 30 is the Monte Carlo result overlaid with the results of the second energy scan. The best fit

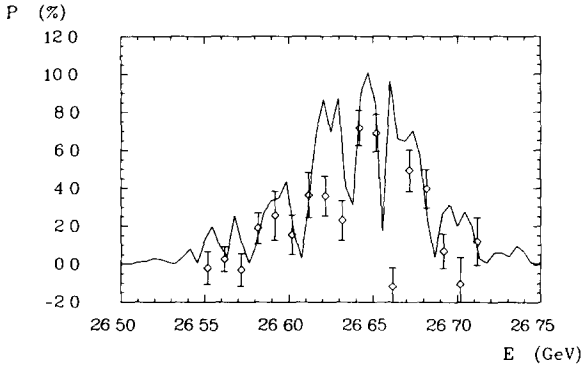

Fig. 30. A measured energy scan (the solid curve in fig. 29) compared to the predictions from the Monte Carlo tracking program. The measured curve has been shifted by -38 MeV. The overall shape is in good agreement, and the drops in the measured polarization have a 30 MeV spacing, as expected from the synchrotron sideband resonances. The height of the predicted curve has been fitted to the data (see the text).

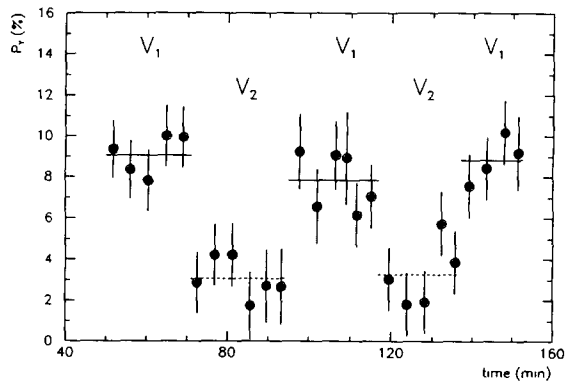

Fig. 31. Beam depolarization by moving the beam into a synchrotron sideband resonance. The polarization is plotted as a function of time, as the amplitude of the rf voltage was switched between $V_1 = 102$ MV and $V_2 = 90$ MV, which reproducibly switched the polarization P_Y between 9% and 3%. The lines are drawn to guide the eye.

(by eye) of the two curves was found by shifting the energy scale of the measured curve down by 38 MeV. This is consistent with the expected uncertainty of ± 50 MeV in the energy scale, which is determined from the dipole field measurements. The polarization scale is a strong function of the orbit errors and these errors cannot be measured well enough to be used in the simulations. To produce a curve which can be qualitatively compared with the measurements, the rms vertical closed orbit distortion of the corrected orbit used in the simulations was larger than that of the beam during the polarization measurements: for the simulations $\sigma_{vco} \approx 1.1$ mm whereas, in reality, for the corrected orbit $\sigma_{vco} \approx 0.7$ mm. Thus the scale of the predictions should be considered a fit to the measured curve. The widths of the bell-shaped curves are in agreement, and the 30 MeV spacing of the dips in the measured polarization is in agreement with the spacing of the synchrotron sideband resonances. The difference in position of the resonance near 26.67 found in the two measurements (see fig. 29) may be due to differences in the synchrotron tune.

If the dips in the polarization are the effects of synchrotron sideband resonances, these resonances can be utilized to depolarize the beam. This is accomplished by changing the amplitude of the 500 MHz sinusoidal accelerating voltage. As in a harmonic oscillator, the frequency of the energy oscillations of the electrons is approximately proportional to the mean value of the square root of the slope of the voltage dV/dt seen by the electron bunch. Increasing the amplitude of the voltage thus increases the oscillation frequency, and so the synchrotron tune, thereby changing the energy spacing of the synchrotron sideband resonances. If the beam energy is set near the position of a resonance, then by changing the amplitude of the

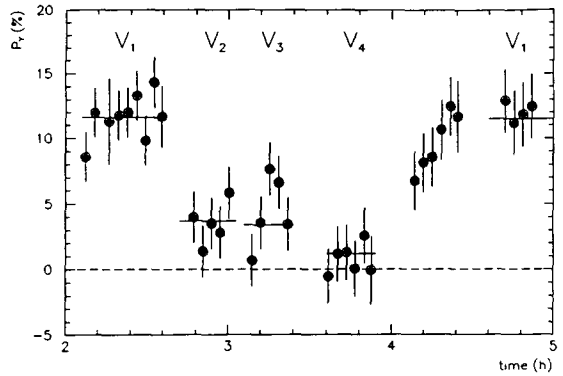

Fig. 32. Beam depolarization by moving the beam into a synchrotron sideband resonance, performed in June 1992. The beam energy was 26.67 GeV. The polarization is plotted as a function of time, as the amplitude of the rf voltage was reduced from $V_1 = 153$ MV to $V_4 = 123$ MV in three steps of 10 MV. The polarization was reduced from its initial value of $12.9 \pm 0.4\%$ to $3.4 \pm 0.9\%$, and at 123 MV the polarization is nearly zero. The voltage was then returned to 153 MV, and the build-up back to $P_Y = 13.0 \pm 2.5\%$ can be seen. The lines are drawn to guide the eye.

voltage the beam can be effectively moved into the resonance, resulting in depolarization.

With the initial voltage of 102 MV a vertical polarization of $9.17 \pm 0.79\%$ was measured: the measured synchrotron frequency f_s was 2.7 kHz, which corresponds to a synchrotron tune Q_s of 0.057. To depolarize the beam the voltage was reduced to 90 MV where the synchrotron frequency was 2.4 kHz, corresponding to $Q_s = 0.051$. The results are plotted in fig. 31. The voltage was changed four times and the polarization was reproducibly switched between about 9% and 3%.

These first measurements indicate the importance of nonlinear depolarizing effects, in particular from higher order synchrotron sideband resonances. They are necessary to explain our measurements with the decoupling bump and the depolarization by coupling the betatron tunes, and the sharp polarization dips in the energy scans. Their effect has been utilized to depolarize the beam by changing the amplitude of the accelerating voltage.

Orbit corrections had been planned to begin optimization of the polarization. Due to lack of time, measurements with only a single correction component at a few strengths were made; the beam energy was 26.67 GeV and the polarization P_Y was 7.34%. No change in the polarization was found.

During the 91/92 winter shutdown, the alignment of the quadrupoles was checked and 13 magnets were found to be misaligned by 1 mm or more. In addition to checking and realigning the quadrupoles, the horizontal and vertical tunes of the electron beam were changed from 47.22 and 47.35, to 47.12 and 47.20, respectively, thus increasing the energy spacing of the first order betatron spin resonances. Subsequent measurements in June 1992 [1] have shown improvements in the polarization, with 15% measured at 26.67 GeV. On the 15th of June, a short energy scan was performed and the beam was successfully depolarized, as during the November measurements, by varying the amplitude of the accelerating voltage. The results of this measurement are shown in fig. 32. The amplitude was changed from 153 MV ($Q_s = 0.074$) to 123 MV ($Q_s = 0.061$) in steps of 10 MV, thereby reducing the polarization from $12.9 \pm 0.4\%$ to $0.9 \pm 0.7\%$. The voltage was then returned to its starting value and the subsequent polarization build-up back to its initial value can be seen.

Parasitic polarization measurements have been made during luminosity runs for the high energy physics experiments. The polarization was consistent with zero within statistical errors. The importance of the compensation of the longitudinal fields of experimental solenoids is shown in a measurement performed on the 15th of April, 1992, when the polarization was mea-

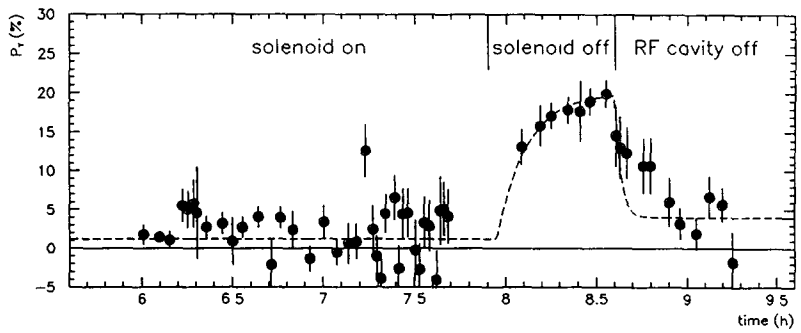

Fig. 33. The depolarizing effect of uncompensated longitudinal fields. The beam energy was 26.67 GeV. The polarization is plotted as a function of time. The measurement started while the ZEUS solenoid was powered without compensation of the field. After the solenoid was turned off, the build-up of polarization is visible, until the loss of power in an rf cavity depolarized the beam. The dashed line is drawn to guide the eye.

sured while the ZEUS solenoid was operating with its compensator off. At this time the proton machine and the H1 solenoids were not operating. As shown in fig. 33, the polarization was consistent with zero while the solenoid was on. The ZEUS operators agreed to turn the solenoid off, and when the measurements were restarted, a build-up of the polarization was seen. The beam was suddenly depolarized when an rf cavity lost power; the maximum polarization reached in the build-up was about 20%.

7. Conclusions, future plans

The construction of the HERA Compton-laser polarimeter for the measurement of the polarization of the electron beam is completed: the laser system delivers the required 10 W circularly polarized photon beam to the electron–photon interaction point, and with the detector and DAQ system we are able to measure the energy and position of the backscattered photons at average rates of up to 100 kHz and provide on-line results to guide the machine operators. At the design electron current the polarization can be measured to an accuracy of 1% in about 12 s.

During the first run of HERA with both the electron and proton rings operational, electron polarization of up to $9.2 \pm 1\%$ was measured. The systematic error is also about 1%. The longitudinal component was small ($< 1\%$). Scans in electron beam energy have been made around 26.66 GeV where the spin tune is a half integer. A bell-shaped curve with sharp dips was found. It is in qualitative agreement with simulations, and the spacing of the measured dips agrees with the predicted spacing of the synchrotron sideband resonances. The synchrotron sideband resonances were successfully used to depolarize the beam by changing the synchrotron tune and pushing the beam into and out-of a resonance. In this way the polarization was reproducibly switched between 9% and 3%. This method was used again in June 1992 to depolarize the beam. Simulations using analytic theory and Monte Carlo tracking programs have been used to interpret the results, and the measured effects are indications of the strong depolarizing effects of higher order synchrotron sideband resonances. Optimization of the polarization using orbit corrections were started.

The results from November 1991 have since been reproduced in spring 1992: after the improvements made in the winter shutdown, polarizations of up to 20% were measured. More recently, in August–October 1992 during which the electron orbit correction scheme was utilized, we have measured polarizations reaching 50–60% and in addition have measured the rise time. Fig. 34 shows a measurement of the polarization build-up time done during September 1992. The curve is a fit by the function (see eq. (1))

$$P(t) = P_{\max}\left[1 - \left(1 - \frac{P_0}{P_{\max}}\right) e^{-(t-t_0)/\tau}\right], \qquad (55)$$

with $P(t)$ being equal to the constant value P_0 for $t < t_0$. The fit results $\tau = 21.8 \pm 4.5$ min and $P_{\max} = 45.2 \pm 2.6\%$, with $\tau_{ST} = 43$ min at the beam energy of 26.7 GeV, confirm the correctness of the calibration of the polarization scale. These most recent results are the subject of another report.

With further dedicated machine time we will continue the study of the orbit correction scheme to increase the polarization further. We plan to improve the depolarization method using resonant spin depolarization. These measurements will first be performed with the "stand-alone" electron ring; later the depolarizing effects of the proton beam, the detector solenoids and compensators, and the feedback system will be measured. A set of spin rotators has been constructed and is ready for installation.

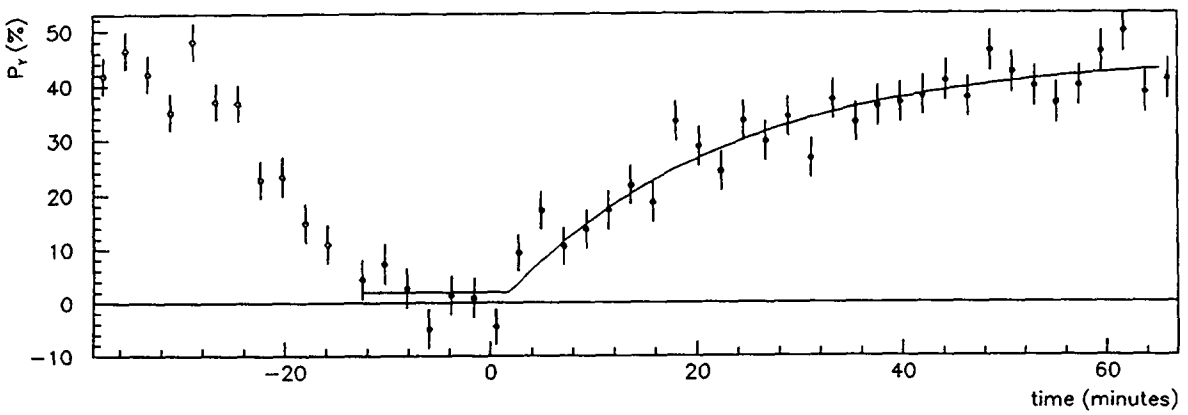

Fig. 34. The measurement of the rise time τ of the polarization at a beam energy of 26.7 GeV. The measurement and the fit are described in a report in preparation.

Acknowledgements

The authors would like to congratulate the HERA machine crew for the excellent performance of HERA and thank them for our good collaboration, with special thanks to W. Bialowons for, in particular, his extensive contributions early in the experiment. We also appreciate the interest and support of Profs. E. Lohrmann, V. Soergel, G.-A. Voß and A. Wagner.

We would like to thank G. Kath, H.-H. Sabath, V. Sturm, and K. Westphal for their work in the design and construction of the calorimeter, and F. Göthe, R. Hamatsu, M. Rohde, and G. Theisen for their help with the optical components of the calorimeter. We thank B. Machowski, S. Ritz, U. Kötz, A. Kotanski, G. Jahnen, and U. Behrens for their help with the data acquisition system.

The collaboration of G. Meyer in the design and construction of many of the components of the polarimeter was indispensable; the assistance of R. Bandelmann is gratefully acknowledged. The design and construction of parts of the readout electronics by N. Bulian, M. Hornung and B. Schaller and of components of the laser transport system by V. Mallinger and the MPI-Heidelberg mechanical workshop are also gratefully acknowledged. We are grateful for the help of T. Romanowski early in the experiment. We thank J.S. Kouptsidis and the Vacuum Group for their assistance in the construction of the modified vacuum chambers; F. Löffler, W. Schwarz and the surveying team. We thank R. Lehmann for his help with the technical drawings. Z. Moroz and D. Toporkov are thanked for their help during data taking.

The contributions of Prof. U. Camerini an the support of the University of Wisconsin are greatly appreciated and warmly acknowledged.

In addition we thank other colleagues from inside and outside DESY for useful advice and assistance, namely G. Alexander, B. Dehning, R. Grimm, G. Kezerashvili, C. Kluth, T. Limberg, M. Placidi, D. Plane, R. Schmidt, Yu. Shatunov, H. Steiner, Yu. Tikhonov, W. Toner and F. Wedtstein.

The Canadian collaborators would like to acknowledge the financial support from NATO and the Natural Sciences and Engineering Research Council.

References

[1] M. Lomperski, The Observation of Electron Spin Polarization at HERA, presented at the 15th Int. Conf. on High Energy Accelerators, Hamburg, July 1992.
[2] The HERA Proposal, DESY HERA Report 81-10 (1981); B. Wiik, in Proc. of the 2nd European Particle Accelerator Conf., Nice, France, June 1990, eds. P. Martin and P. Mandrillon (Edition Frontières, 1990).
[3] ZEUS Collaboration, Technical Proposal for the ZEUS Detector, DESY Report (1986).
[4] H1 Collaboration, Technical Proposal for the H1 Detector, DESY Report (1986).
[5] A.A. Sokolov and I.M. Ternov, Sov. Phys. Doklady 8 (1964) 1203;
I.M. Ternov, Yu.M. Loskutov and L.I. Korovina, Sov. Phys. JETP 14 (1962) 921.
[6] A.W. Chao, Nucl. Instr. and Meth. 180 (1981) 29;
also in: AIP Conf. Proc. 87 (1982) 395.
[7] Ya.S. Derbenev and A.M. Kondratenko, Sov. Phys. JETP 37 (1973) 968.
[8] S.R. Mane, Phys. Rev. A36 (1987) 105.
[9] D.P. Barber, in: Proc. of the 9th Int. Symp. on High Energy Spin Physics, Bonn, September 1990, eds. K.-H. Althoff and W. Mayer (Springer, 1991);
D.P. Barber, in: Proc. of the 2nd European Particle Accelerator Conf., Nice, France, June 1990, eds. P. Marin and P. Mandrillon (Edition Frontières, 1990).
[10] B.W. Montague, Phys. Rep. 113 (1984) 1.
[11] W.W. MacKay et al., Phys. Rev. D29 (1984) 2483.
[12] J.R. Johnson et al., Nucl. Instr. and Meth. 204 (1983) 261.
[13] A.E. Blinov, Nucl. Instr. and Meth. A241 (1985) 80.
[14] H.D. Bremer et al., DESY Report 82-026 (1982);
D.P. Barber et al., Phys. Lett. B135 (1984) 498.
[15] L. Knudsen et al., Phys. Lett. B270 (1991) 97.
[16] K. Nakajima et al., Phys. Rev. Lett. 66 (1991) 1697.
[17] J. Buon and K. Steffen, Nucl. Instr. and Meth. A245 (1986) 248.
[18] L. Thomas, Philos. Mag. 3 (1927) 1;
V. Bargmann, L. Michel and V.L. Telegdi, Phys. Rev. Lett. 2 (1959) 435.
[19] D.P. Barber et al., DESY Report 85-044 (1985).
[20] J. Kewisch et al., Phys. Rev. Lett. 62 (1989) 419.
[21] D. Blockus et al., SLAC-Proposal-SLC-Upgrade-01 (1986).
[22] M. Placidi and R. Rossmanith, Nucl. Instr. and Meth. A274 (1989) 79.
[23] U. Fano, J. Op. Soc. Am. 39 (1949) 859.
[24] M. Born and E. Wolf, Principles of Optics (Pergamon Press, 1959).
[25] M. Sands, SLAC-0121 (1970).
[26] D.P. Barber et al., DESY HERA 86-05 (1986).
[27] D.P. Barber et al., DESY HERA 90-19 (1990).
[28] A. Mücklich, diploma thesis, University of Heidelberg (1992).
[29] T. Suzuki, KEK-76-3 (1976).
[30] R. Kaiser, diploma thesis, University of Münster, Germany, DESY F35D-92-02 (1992).
[31] M. Lomperski, Ph.D. thesis, University of Wisconsin, Madison, in preparation.
[32] H. Götschel, diploma thesis, University of Hamburg, Germany, DESY F35D-90-01 (1990).
[33] H. Gressmann, diploma thesis, University of Hamburg, Germany (1991).
[34] Ch. Büscher, diploma thesis, University of Heidelberg (1992).

[35] A. Caldwell et al., ZEUS Note 92-022 (1992).
[36] Y.S. Tsai, Rev. Mod. Phys. 46 (1974) 815.
[37] W.R. Nelson, H. Hirayama and D.W.O. Rogers, SLAC-265 (1985).
[38] V.I. Telnov, Nucl. Instr. and Meth. A260 (1987) 304; B. Dehning et al., Phys. Lett. B249 (1990) 145.
[39] J.J. Hernandez et al., Phys. Lett. 239 (1990) 1.
[40] M. Böge, ed. F. Willeke, DESY HERA 92-07 (1992).